



TAMPEREEN TEKNILLINEN YLIOPISTO  
TAMPERE UNIVERSITY OF TECHNOLOGY

DEVANAND ARULPRAGASAM

Investigation of scintillation effects in European Galileo Signals

MASTER OF SCIENCE THESIS

Subject approved by Department Council  
09/11/2016

Examiner: Assoc. Prof. Elena Simona  
Lohan

## ABSTRACT

TAMPERE UNIVERSITY OF TECHNOLOGY

Master's Degree Program in Electrical Engineering

**ARULPRAGASAM, DEVANAND:** Investigation of scintillation effects in European Galileo signals.

Master of Science Thesis, 65 pages

May 2017

Major: Wireless Communications

Examiner: Assoc. Prof. Elena Simona Lohan

Keywords: Scintillation, GNSS impairments, Channel Model.

Ionospheric scintillations are known to be rather challenging in Global Navigation Satellite Systems (GNSS) receivers. The scintillation effects include rapid variations in signal phase and amplitude, which may hinder the receiver to acquire and track the signal and may cause a loss of lock at GNSS receiver. This thesis focuses on the scintillation effects on the European GNSS namely, Galileo. Abrupt phase variations during transmission cause deep power fades called canonical fading, half cycle slips and frequency unlock. Phase locked loop designs that are currently available helps in reducing the scintillation effects to some extent, though this is complicated when scintillation is severe.

This thesis focuses on investigating some of the scintillation effects on Galileo signal during acquisition. The considered performance criteria are the detection performance and the root mean square error at the receiver. For implementing this task, this thesis uses two toolboxes, namely Cornell Scintillation toolbox for generating synthetic scintillation time histories and TUT MBOC tracking model for simulating and studying the scintillation effects at the receiver. Cornell Scintillation toolbox generates synthetic amplitude and phase time histories based on two input parameters namely, scintillation intensity and decorrelation time that show how rapidly the signal amplitude and phase change. TUT MBOC acquisition and tracking simulator generates Galileo E1 signal that undergoes MBOC modulation and it is transmitted through multipath Nakagami-m fading channels.

The thesis work focused on merging the scintillation time histories generated by Cornell scintillation toolbox with the TUT MBOC acquisition tracking algorithm, by adding the scintillation to fading channel. By calculating the Line of Sight (LOS) phase delay, the acquisition of the received signal is performed with and without scintillations. The obtained results with and without scintillations are compared and studied in order to evaluate the impact of scintillations on the European GNSS.

## PREFACE

This Master of Science Thesis has been written for the Department of Electrical Engineering at the Tampere University of University, Tampere, Finland.

I would like to express my gratitude to my wonderful supervisor **Asst. Prof. Elena-Simona Lohan** for her guide and support, throughout the thesis work. I would like to thank my friends in Finland for their support during my Master of Science studies.

My special thanks to my family members in India for their love and support and I dedicate this M.Sc. Degree to the memory of my Mother.

Tampere, Finland

Devanand Arulpragasam

## TABLE OF CONTENTS

ABSTRACT.....	ii
PREFACE.....	iii
LIST OF TERMS AND ABBREVIATIONS.....	vi
1. INTRODUCTION.....	9
1.1 Background and motivation.....	9
1.2 Thesis aims.....	10
1.3 Author’s contributions.....	11
1.4 Thesis structure.....	11
2. GNSS – BRIEF INTRODUCTION.....	13
3. SPACE WEATHER AND ITS EFFECTS ON GPS SIGNALS.....	15
3.1 Ionospheric regions and weather.....	15
3.1.1 Equatorial and low latitude regions.....	15
3.1.2 Mid-latitude region.....	17
3.1.3 High latitude region.....	18
3.2 Effects of solar activity on GPS.....	19
3.3 Ionospheric impacts on GNSS signals.....	20
4. CHARACTERIZATION OF SEVERE SCINTILLATION EFFECTS ON GNSS.....	23
4.1 The empirical scintillation library.....	23
4.2 Characteristics of strong scintillation.....	25
4.2.1 Scintillation severity.....	25
4.2.2 Power phase spectra and first-order statistics.....	28
4.2.3 Canonical fading.....	30
4.3 Scintillation effects on Acquisition.....	31
4.3.1 Parallel FFT based circular correlation.....	31
4.3.2 Detection probability and performance.....	33
4.4 Scintillation effects on code tracking loops.....	34
5. CORNELL SCINTILLATION MODEL.....	35
5.1 Scintillation model.....	35
5.1.1 Amplitude distributions.....	36
5.1.2 Autocorrelation function of the scintillation model.....	39
5.2 Scintillation simulator mechanization.....	42
5.3 Model validation and conclusion.....	43
5.4 Various other scintillation models: benefits and drawbacks.....	44
5.4.1 Automatic ionospheric scintillation detector for GNSS.....	44
5.4.2 Modernized GNSS ionospheric scintillation and TEC Monitoring... ..	44
5.4.3 Simulating ionospheric scintillation effects using low complexity technique.....	44
6. GALILEO SYSTEM - OVERVIEW.....	46
6.1 Galileo signal characteristics.....	46
6.2 Galileo Signal Modulation – MBOC.....	46

6.2.1	BOC Modulation.....	46
6.2.2	MBOC Modulation.....	47
6.2.3	CBOC Modulation.....	47
6.3	TUT MBOC Simulator .....	47
7.	RESULTS AND DISCUSSION .....	50
7.1	Performance analysis of scintillated E1 signal.....	50
7.2	Impact of multipath fading channels.....	52
7.3	Performance analysis of different scintillation levels .....	55
7.3.1	Analysis of scintillation levels with fading.....	55
7.3.2	Analysis of scintillation levels without fading .....	57
8.	CONCLUSION .....	60
	REFERENCES.....	61

## LIST OF TERMS AND ABBREVIATIONS

$R_{\xi}(t)$	Autocorrelation function
$ H(f) $	Amplitude Response function
$N_B$	BOC Modulation Order
$\rho$	Charge Density
$q$	Charge of Electron
$f_c$	Chip frequency
$T_I$	Coherent Integration Time
$d_{\tau}(t)$	Data Bit
$\tau_0$	Decorrelation Time
$f_d$	Doppler offset
$E[.]$	Expected value
$\Gamma(.)$	Gamma Function
$c_{\tau}(t)$	GNSS reference code
$\delta t$	Group Delay
$n_e$	Ionospheric Electron Density
$m_e$	Mass of Electron
$N_s$	Oversampling factor
$\epsilon$	Permittivity
$\Delta\theta$	Phase Change
$\sigma_{\phi}^2$	Phase error variance
$v_{\phi}$	Phase Velocity
$\omega_{pe}$	Plasma Frequency
$T$	Power Density
$K$	Ricean Parameter
$S_4$	Scintillation Index
$I$	Signal Intensity
$C$	Speed of Light
$f_{sc}$	Sub-carrier frequency
$\langle . \rangle$	Time Average
$v_g$	Wave Group Velocity
ACF	Auto Correlation Function
AWGN	Additional White Gaussian Noise
BOC	Binary Offset Carrier
BPSK	Binary Phase Shift Keying
CNR	Carrier to Noise Ratio
C/A	Coarse Acquisition
CDMA	Code Division Multiple Access
CBOC	Composite Binary Offset Carrier

CosBOC	Cosine Binary Offset Carrier
dB	Decibel
DNA	Defence Nuclear Agency
DOF	Degree of Freedom
DLL	Delay Lock Loop
ESL	Empirical Scintillation Library
EU	European Union
FFT	Fast Fourier Transform
GEO	Geo Stationary Orbit
GHz	Giga-Hertz
GNSS	Global Navigation Satellite System
GLONASS	Global Orbiting Navigation Satellite System
GPS	Global Positioning System
Hz	Hertz
HHT	Hilbert-Huang Transform
I	In-phase
IF	Intermediate Frequency
keV	Kilo-electron Volt
LOS	Line of Sight
MEO	Medium Earth Orbit
MEDLL	Multipath Estimating Delay Lock Loop
MBOC	Multiplexed Binary Offset Carrier
nT	NanoTeslas
NY	New York
NP	Neyman-Pearson
PLL	Phase Lock Loop
PVT	Position, Velocity and Time
PSD	Power Spectral Density
PDF	Probability Density Function
PRN	Pseudo Random Noise
Q	Quadrature
RMSE	Root Mean Square Error
SBAS	Satellite Based Augmentation System
STL	Scalar Tracking Loop
SNR	Signal to Noise Ratio
SinBOC	Sine Binary Offset Carrier
SFU	Solar Flux Unit
TECU	TEC Unit
TMBOC	Time Multiplexed Binary Offset Carrier
TEC	Total Electron Content
UHF	Ultra High Frequency
uV	Ultra Violet

UT	Universal Time
UT	Utah
VDFLL	Vector Delay/Frequency Lock Loop
VHF	Very High Frequency
WAAS	Wide Area Augmentation System

# 1. INTRODUCTION

## 1.1 Background and motivation

Ionospheric scintillations are the irregularities caused during the signal transmission from satellite to the GNSS receivers. Unlike radio waves striking nearby surfaces of antenna, the satellite radio waves also undergo multipath transmission when travelling through space. During the wireless transmission, the signal undergoes two main types of effects, namely refraction and diffraction. In the ionospheric layer (which is from 50 to 400 KM above the Earth), the GNSS signal passes through free electrons along the path. This causes rapid phase shifts and variations in the signal's group delay. This effect is called signal refraction. When the length of ionospheric irregularities extend upto 400 meters, then the GNSS signal scatters and it reaches the GNSS receiver through multiple paths. All the received signals are added constructively or destructively at the receiver and this causes large variations in signal amplitude and phase. This effect is called signal diffraction. These two effects, caused by signal refraction and diffraction, are called scintillation. More errors occur at the receiver due to signal diffraction and are quite challenging comparing to the effects of signal refraction. Signal diffraction causes rapid phase shifts and fades the signal power to more than 30 dB – Hz. [1]

Troposphere, at its turn, introduces also some scintillation in receiver but the effects of tropospheric errors are less comparing to the ones caused by the ionospheric scintillations. Ionospheric multipath errors are high in mobile receivers as the geometry of path from satellite to receiver is constantly varying. Multipath errors are less in static receiver applications than in dynamic receiver applications, and the errors are mitigated by the techniques involving the citation of redundant geometry path from satellite to receivers. Background ionosphere corrections are possible using dual frequency or differential methods. [2]

Although dual frequency and differential methods enable the background ionospheric correction, ionospheric irregularities such as rapid change in phase shifts and group delay measurements remains and may decrease the accuracy of GNSS receiver measurements. Also ionospheric scintillation may lead to loss of lock on satellites which results in lost positioning service or decreased positioning accuracy. Phase locked loops (PLL) and delay locked loops (DLL) designs available at GNSS receiver helps reduce the scintillations to certain extent. The estimation of the effect of scintillation must be carried out during the signal travelling through ionosphere as well

as during the post processing effect of receiver. This estimation of scintillation effects is done in terms of loss of lock and reduced accuracy for various times and conditions. [2]

The geographical regions also determine the strength of scintillation effects at GNSS receiver. Strong scintillation, for almost one hour, is possible at equatorial region during evening until midnight [2]. During this period, scintillations are lesser in Pacific regions in the American, African and Indian longitudes from April to August whereas strong scintillation occurs in Pacific region. These scintillation effects are exactly opposite during the period from September to March in the longitudes. Mild scintillation is possible in equatorial latitudes provided the effect lasts longer. In polar and auroral regions, considerable effects of scintillation occur especially due to northern lights. [2]

## 1.2 Thesis aims

In order to mitigate the scintillations at GNSS receiver, various scintillation models were created and simulated with GNSS signal simulator. The scintillation models with statistical data were compared with the data gathered from GNSS receiver and simulated with GNSS signal simulator [1]. The simulation results were obtained and studied to discuss cause and effect of scintillations at GPS receiver.

The aims of this thesis have been:

1. To implement scintillation channel model suitable for Galileo GNSS and based on the Cornell matlab scintillation model.
2. To study and understand the Galileo modulation used in Galileo Open Service, namely Multiplex Binary Offset Carrier (MBOC) modulation and its corresponding acquisition and tracking model with multipath to simulate and estimate delays and noise at the receiver.
3. To merge Cornell scintillation model with the MBOC tracking model for simulating the results with and without scintillations.

The overall aim of this thesis has been to investigate and gain knowledge about various impairments in GNSS receivers such as multipaths, ionosphere, scintillations and so on. Apart from understanding Cornell scintillation model, various other scintillation models are also analysed through literature review to know the benefits and drawbacks of the models. The focus of this study is on the scintillation channel model of European satellite navigation system GALILEO. As stated above, scintillation mitigation models of all other satellite navigation systems, GPS, BEIDOU and GLONASS will also be analysed and studied. This provides us the knowledge of current techniques and models that helps in mitigating the scintillations involved in all the satellite navigation systems.

### 1.3 Author's contributions

The thesis contributions are summarized below:

- A detailed research of the scintillation effects at GNSS receivers namely, multipaths and ionospheric effects.
- A study of the concept of Cornell scintillation toolbox that generates synthetic scintillation histories to merge with TUT Galileo simulator.
- Understanding TUT Galileo simulator that uses MBOC modulation to test and simulate results for estimating and learning the phase delay effects during acquisition and tracking.
- Running basic tests with the merged simulator to investigate the effect of scintillations on the Galileo receiver performance.

### 1.4 Thesis structure

This thesis has been structured in the following way to present the complete view of the research:

**Chapter 1** of this thesis outlines the brief introduction of the objectives of the research followed by author's contributions and thesis structure.

**Chapter 2** offers a short explanation about Global Navigation Satellite Systems (GNSS) and provides basic information about signal processing tasks such as acquisition, tracking and navigation solution computation.

**Chapter 3** provides information about space weather factors such as solar activity and magnetic storms and possible geographical locations where scintillations affect the GNSS signals.

**Chapter 4** explains in detail the characteristics of strong scintillation and the scintillation effects on acquisition and tracking loops.

**Chapter 5** introduces Cornell scintillation model and its mechanization that simulates and generates synthetic scintillation time histories. It also analyses complex equatorial scintillation that causes tracking difficulties and validates the scintillation effects through amplitude distributions and power spectra.

**Chapter 6** explains TUT MBOC simulator, a Galileo satellite system which is used for acquisition and tracking purposes. Synthetic scintillation histories generated from Cornell Scintillation toolbox are merged with the TUT MBOC simulator. The

scintillated Galileo E1 signals are then transmitted over multipath Nakagami-m fading channel to analyse the receiver results by calculating Line of Sight (LOS) delay.

**Chapter 7** shows the performance of MBOC tracking algorithm through simulation results obtained in terms of detection probability for acquisition and Root Mean Square Error (RMSE) for tracking. Simulation results are also obtained and compared for different scintillation intensities namely, strong, moderate and weak scintillations.

**Chapter 8** concludes the thesis with the conclusion drawn from the entire research and simulations.

## 2. GNSS – BRIEF INTRODUCTION

Global navigation satellite system is a group of satellite systems that offers global coverage and navigation information worldwide. GNSS provides good accuracy outdoors and is essential in applications such as weather research, earth science, aviation and agricultural science [3]. Currently, four global satellite navigation systems available worldwide, namely, Galileo built with European funding, GPS NAVSTAR built and operated by USA, GLONASS, operated by Russia, and BeiDou Navigation Satellite System of China. The quality of service offered by satellites depends on criterias such as accuracy, integrity, continuity and availability [4]. The principle of satellite positioning system enables us to locate the position of user in terms of latitude, longitude and height. This is possible through taking into consideration the ranges or range differences between user and satellites. [5]

The increased requirements for location-based services are aiming to provide a unique system that is combination of all global navigation satellite systems [6]. Therefore, concepts and techniques used in different navigation satellite systems have to be compatible and interoperable. This ensures that people all around the world, irrespective of their nationalities, utilize GNSS services, safely and conveniently [7]. Choosing correct frequency is important to transmit signal to receiver without loss. GNSS uses L-band in the frequency spectrum and wavelength ranges from 15 to 30 cm. Carrier frequency is selected between 100 MHz and 10 GHz, as ionospheric delays and errors due to various atmospheric effects are much higher in higher frequency ranges, and lower frequency ranges are heavily used by other mobile applications. Choosing high frequencies with high available bandwidth is essential for modulating carrier frequency with pseudorandom noise (PRN). [8]

GNSS receiver operation is carried out by choosing a channel for each satellite and performing the signal processing tasks, namely acquisition, tracking and navigation solution computation. In order to allocate the channel, a GNSS receiver searches for visible satellites and this process of identifying satellites is known as *Acquisition*. The two important parameters of acquisition are *Frequency* and *Code Phase*. Based on determining the maximum value of these parameters, a satellite is identified with its corresponding frequency and code phase. If all the values are same and so the maximum value is not found, then the satellite is not visible to user. These parameters are updated frequently, as the signal properties vary with time. The process of checking and refining the values of frequency and codephase is called *Tracking*. It involves two parts:- the

first part is the code tracking, and second part is the carrier frequency or phase tracking. Hence, tracking is done frequently to check the changes in frequency and if the receiver stops tracking satellites then acquisition is done again for those satellites. [9]

In order to compute the distance between the satellite and user's receiver, also called pseudorange measurements, two common methods are used, namely common transmission line and common reception time. All the clocks on the satellites are synchronized to each other in GNSS so that the pseudorange can be calculated as the time or distance between two reference points. The two methods use different way to select reference point [10]. In the first method, satellite tracked with shortest time is considered as common transmitter time and is taken as reference. The relative pseudoranges of other satellites are computed by estimating relative time difference by the receiver with respect to the reference time of shortest channel. In the second method, common receiving time or distance is set as reference time. The receiver estimates elapsed time or delays of all tracked satellites with respect to reference time. After pseudorange computation, Position, Velocity and time (PVT) computation is done to calculate user's location. To compute the PVT of the satellite, the receiver requires ephemeris data and time of transmission that are embedded in the navigation message. [10]

### **3. SPACE WEATHER AND ITS EFFECTS ON GPS SIGNALS**

Space weather is one of the factors that affect the radio waves received by GNSS receivers. The space weather impact on the GNSS signals occur because of the solar activity, when solar flare leads to solar radio bursts. Solar flares annihilate the solar magnetic field and it produces energy in the form of ultraviolet rays, x-rays, coronal mass ejections and large solar winds. A strong magnetic storm is produced when the energy particles reaches the surface of earth. Due to this, Van Allen radiation belts change [11] and create plasma of 100 kiloelectronvolts (keV) surrounding the earth causing harm to Geo Stationary Orbit (GEO) and Medium Earth Orbit (MEO) space vehicles. The factors such as magnetic storms and disturbances in the Earth's magnetic field create scattering of radio waves in ionosphere and produce scintillations. The effect on GNSS signals increases during a solar maximum, when ultraviolet radiation increases the density and thickness of ionosphere through ionization. [11]

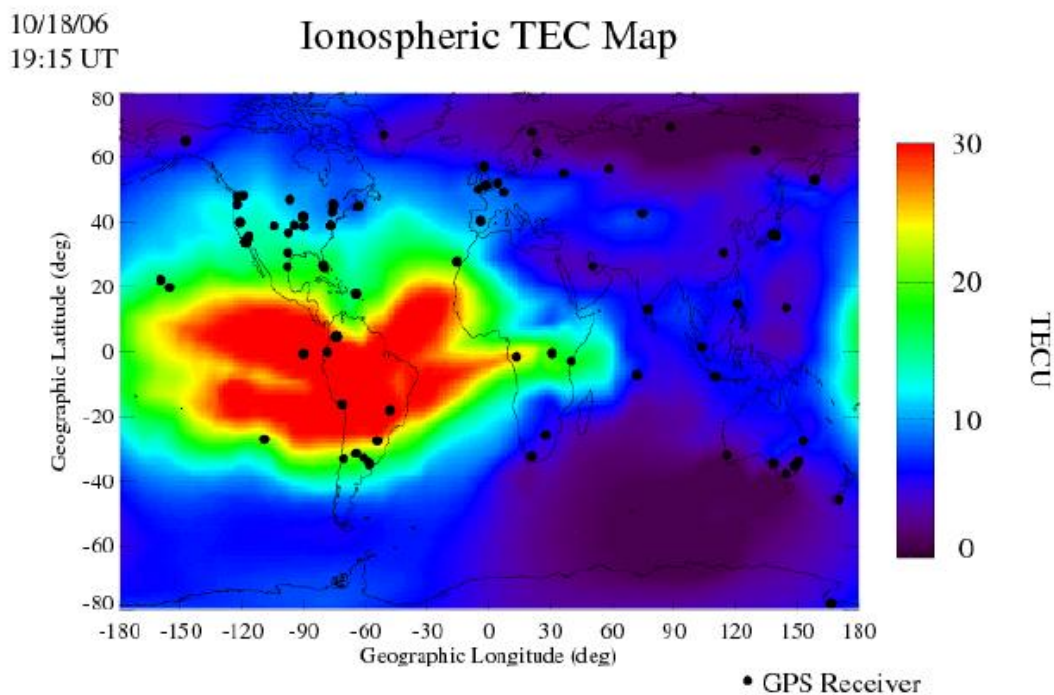
#### **3.1 Ionospheric regions and weather**

GNSS signals are affected by scintillations caused by four different categories of space weather. An important cause of the disturbance is Solar ultraviolet (uV) that arise during solar maximum and creates thicker and denser ionosphere due to direct ionization. The above mentioned ionospheric effect strongly affects the GNSS signals at equatorial and tropical latitudes. Ionospheric impact is stronger at mid latitudes than at higher latitudes, as a result of magnetic storms. At high latitudes northern lights produces ionosphere that affects the GNSS signals lesser at mid and low latitudes. Solar radio bursts affects the GNSS signals by introducing noise at the receiver in the range of 1.2 GHz to 1.6 GHz. [11]

##### **3.1.1 Equatorial and low latitude regions**

Figure 3.1, reprinted with permission from [11] shows different aspects of equatorial ionosphere. During the day, the bands with peak Total Electron Content (TEC) values are formed at about 15 degrees latitudes on both side of geomagnetic equator, and this is known as Appleton or equatorial anomalies. TEC is the number of free electron along a rectangular solid tube of one meter squared cross section. TEC values are expressed in TEC unit (TECU) [12]. The increasing ionospheric plasma at the equator causes anomalies by moving the magnetic field lines to higher latitudes. These bands with anomalies increase the ionospheric electron densities and the phenomenon sometimes

causes scintillations during signal transmission to GNSS receiver. During the night, ionospheric plasma at the equator remains accumulated in the ionosphere and it causes bubbles that rise from few hundred to thousand kilometres. This condition is referred to as Rayleigh-Taylor instability [11]. The upward movement of bubbles occurs for about an hour along the magnetic field lines, causing scintillations in the form of ionospheric irregularities and electron density gradients.



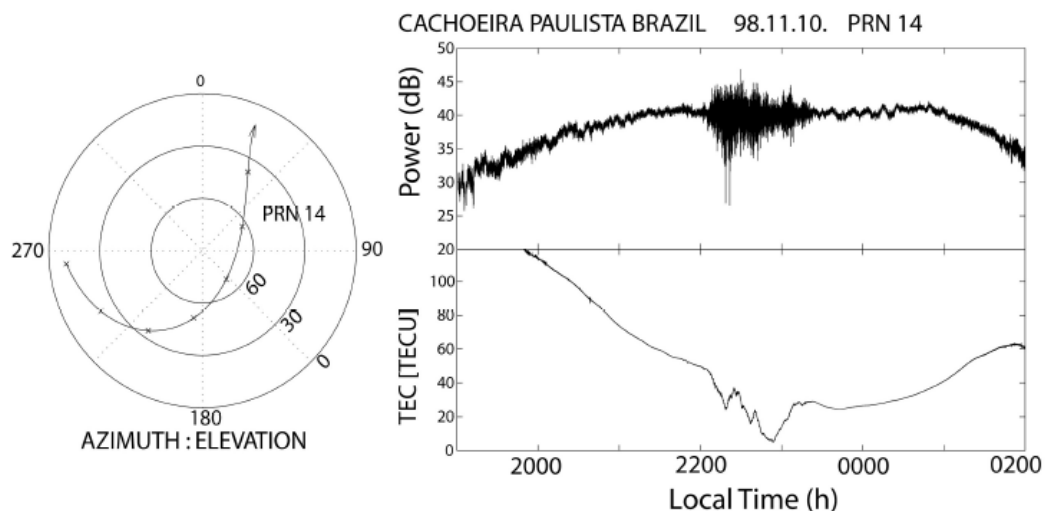
**Figure 3.1:** *Model of Global Ionospheric TEC Map. Reprinted with permission from [13]*

Figure 3.2 shows an example of equatorial ionospheric bubble and the corresponding amplitude scintillations. The figure shows the elevation-azimuth plot of GPS signal PRN 14 on the left hand side and the record of signal power and TEC on the right hand side. The plot illustrates that the TEC values in the ionosphere are larger at the elevation of the satellites and when the GPS signal passes through ionospheric bubble, the TEC values are suppressed and decreased. When the signal exits the bubble, the TEC value becomes larger as the elevation goes down. The GPS signal in the upper right side of the figure shows the increase in amplitude during the rise of satellites in elevation and it is the result of antenna gain pattern. When the signal enters the bubble, the constant fluctuations of amplitude are observed which results in scintillation. Though this example highlights the moderate event, scintillations can be much more extensive and technicians should not assume that the scintillations occur only for the brief period.

In short, ionospheric bubbles and the corresponding scintillations occur more often after sunset. In a climatological point of view, chances of occurrence of bubbles are more when magnetic field lines are in darkness. Moreover, for geographical regions,

bubbles occur during the month of September and March when geographical longitude lines and magnetic longitude lines are parallel. When the lines are not parallel, bubbles occur during the months from November to February.

GNSS signals are also affected with severe solar uV intensity frequently at tropical or low latitudes but the effects are minimized due to the occurrence of magnetic and solar storms at tropical region. Space weather effects on GNSS signals are similar for equatorial or low latitude regions. [11]



**Figure 3.2:** Illustration of an equatorial ionospheric bubble and corresponding amplitude scintillations. Reprinted with permission from [13]

### 3.1.2 Mid-latitude region

Mid latitudes are generally neglected by scientists, as the active regions in mid latitudes are lower compared to high latitude and low latitude regions. In recent times, imaging of mid latitude regions were carried out, in order to study the ionospheric storms and the changes in ionosphere. Magnetic storms increase the electron density gradient and introduce irregularities in the ionosphere that in turn causes scintillation in the signals. The first observation was made at Ithaca, NY when the magnetic storms were low and the GPS receiver underwent loss of lock due to scintillating signals. The observation details are shown in Figure 3.3, reproduced with permission from [11]. This figure consists of three panels, upper, middle and lower panels showing the measurement results of magnetic storm strength ( $D_{st}$ ), the received signal power ( $C/N_0$ ), and TEC values respectively.

In the upper panel, the maximum negative value was shown as -100 nanoteslas (nT) and higher negative value indicates more stronger magnetic storms. The middle panel displays the scintillations of GPS signal from 2400 Universal Time (UT) and the

signal distortion continues until 2730 UT. The lower panel displays the large variations in TEC value near 2400 UT and the TEC values during scintillation were almost half the normal value when observed without signal distortions.

### 3.1.3 High latitude region

High latitude ionosphere is the medium structured with high electron density gradients of larger magnitude. The ionospheric impacts at high latitude regions are mainly due to solar activity and effects of magnetic field of the earth associated to the solar wind. Charged particles penetrations in the northern area are observed when aurora, or the northern lights, occurs. The outbreak of the auroral arc causes the charged particles to precipitate at higher intensities and infrequently affects the GNSS signals causing scintillations due to solar wind.

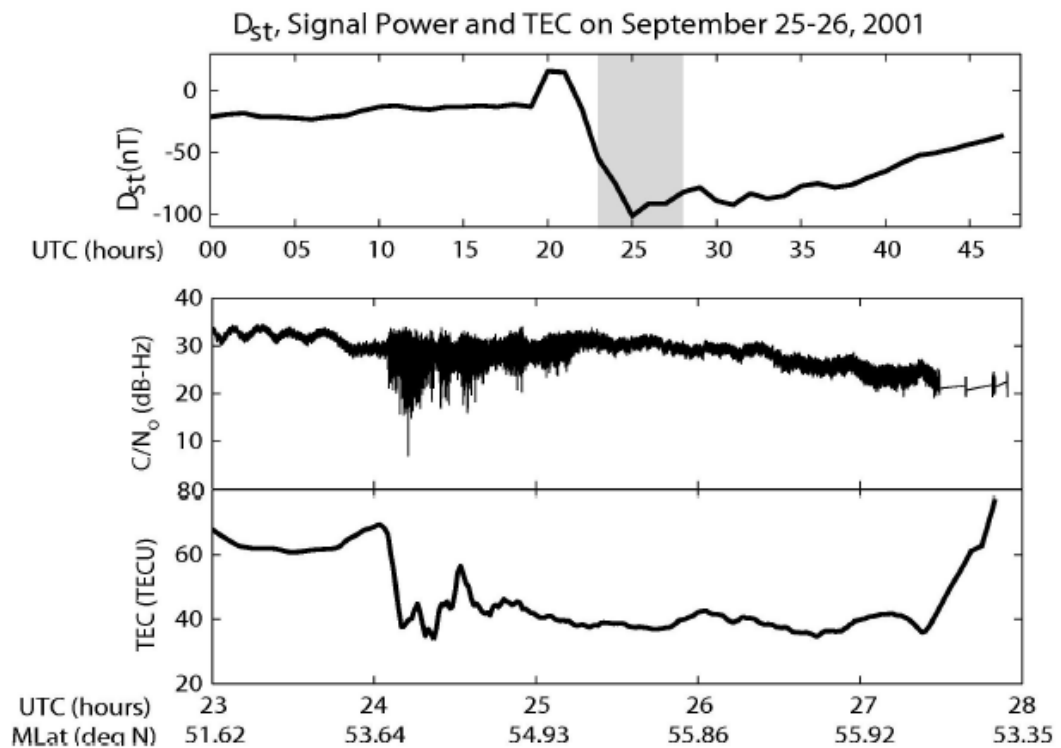


**Figure 3.3:** Observation results of scintillations at mid latitude region, Ithaca, NY. Reprinted with permission from [13]

Apart from the northern lights, magnetic substorms, flares or coronal mass ejections are the main causes of scintillations at high latitude regions such as Nordic European area. TEC rate of change index is associated to strong scintillations and causes position errors in GNSS and receiver loss of lock. To correct these errors, improved models on high latitude phenomena are required for GNSS based applications and studies focus currently on research of the models with additional features. High latitude space weather corresponds to Very High Frequency (VHF) and Ultra High

Frequency (UHF) frequencies and not at L-band frequencies. Therefore, the electron density change does not affect the GNSS signals at these frequencies. [13] [14]

### 3.2 Effects of solar activity on GPS

Solar activity is an important aspect in space weather and solar maximum occurs once in every 11 years that increases the solar magnetic field [11]. The solar magnetic fields are disturbed by solar flares, a sudden burst of radiation released from the surface of the sun [15], during the sunspot maximum and energy are released in various forms such as x-rays, stormy solar winds, solar uV light, energetic particles (protons) and coronal mass ejections. During solar flares, broadband solar radio bursts are introduced at the range of 0.1 to 10 GHz. Until December 6, 2006, solar radio bursts were not intense and the intensity increased to 1,000,000 Solar Flux Units (SFU), ( $1 \text{ SFU} = 10^{-22}$  watt per square meter per hertz ( $\text{Wm}^{-2} \text{ Hz}^{-1}$ )). This increase is more than 100 times higher than previous solar radio bursts during sunspot maximum.

Figure 3.4 displays the spectrum of solar radio bursts in the top panel, and the value of spectrum ranges from 1 GHz to 2 GHz and the bottom panel shows the  $C/N_0$  at Wide Area Augmentation System (WAAS) receiver located at Houston. The solar radio burst spectrum in the top panel of the figure starts at 1850 UT and extends till 1950 UT. The  $C/N_0$  values in the bottom panel are shown in red when the signal was recorded during intense solar radio bursts and blue line readings were recorded a day before the occurrence of solar radio bursts. The  $C/N_0$  value reduces due to the scintillation and the signal distortion occurred for almost 45 minutes. The robust WAAS receiver mitigated the signal distortions using atomic clocks and phase locked loops to decrease phase noise in an effective way. Furthermore, all GPS signals were distorted strongly for single-frequency receivers, and minimal impacts such as loss of lock were observed in receivers such as less robust, semi-codeless and dual-frequency receivers during the event of solar radio bursts. Operational monitors are responsible for observing the solar radio bursts and reduced power levels at the receiver. If the intensities of solar radio bursts were not recorded, then the chances are that more GPS receivers would be affected in next solar maximum. [13] [16]

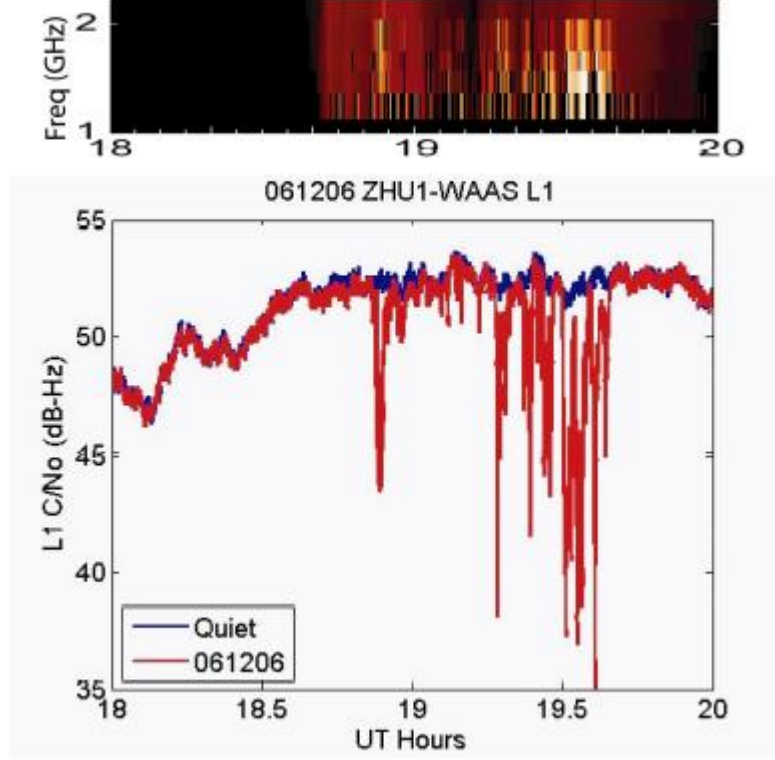


**Figure 3.4:** Received signal power level readings ( $C/N_0$ ) before and during the intense solar radio burst. Reprinted with permission from [16]

### 3.3 Ionospheric impacts on GNSS signals

The main cause of scintillations is the scattering of GNSS signals in ionosphere. The plasma present in the ionosphere affects the signals in three ways [12]. Firstly, code delay occurs when the group velocity decreases and wave group velocity  $v_g$  is given by,

$$v_g = \sqrt{[(1 - \omega_{pe}^2) / (\omega^2)]} \quad (3.1)$$

where,  $\omega_{pe}$  is plasma frequency with value (6.28 – 62.8 rad/s) is given by,

$$\omega_{pe} = \sqrt{[n_e q^2 / \epsilon m_e]} \quad (3.2)$$

where,  $n_e$  is ionospheric electron density,  $q$  is the charge of electron and  $m_e$  is mass of electron in ionosphere and  $\epsilon$  is permittivity. Secondly, the value of phase  $v_\phi$  increases when phase velocity increases and is denoted by,

$$v_\phi = c / \sqrt{[(1 - \omega_{pe}^2) / (\omega^2)]} \quad (3.3)$$

Thirdly, irregularities in density of plasma present in ionosphere scatters the radio waves. The scale length is similar to Fresnel length and the value is about 350m or more

for GNSS signals. In the above equations of phase velocity and group velocity, ionospheric electron density is the only variable parameter and so the value of group delay  $\delta t$  and change in phase can be estimated by integrating electron density with respect to signal path,

$$\delta t = [q^2 / (2c \epsilon m_e f^2 (2\pi)^2)] \int_p n_e dp \quad (3.4)$$

where the integral part in the above equation represents total electron content (TEC),  $c$  is speed of light,  $f$  is frequency and  $\rho$  is charge density. TEC is mostly contributed by ionospheric plasma, as the electron density is higher in ionosphere, and therefore the equation can be simplified in terms of meter-square as,

$$\delta t = [40.3 / (c f^2)] * (\text{TEC}) \quad (3.5)$$

The amplitude scintillations are identified through the amplitude fluctuations. Constructive interference occurs during increase in amplitude and destructive interference occurs during decrease in amplitude. Figure 3.5 shows the example of destructive interference when two GPS signals are tracked at the same time, with PRN 8 not scintillating while PRN 7 scintillates with fading of upto 40 dB. The GPS signals are received using digital storage receiver of mass memory at the rate of 5.7 Msamples/s and analysed using Matlab software receiver, as the hardware receiver fails to track when carrier-to-noise ratio reaches 27dB. Kalmar tracking loop enables the scintillated GPS signal to be tracked and processed. GPS receivers performs acquisition along with the tracking of signal phase or frequency. Phase lock loops are weak when the received signal contains deep fades with half-cycle phase flips. Three important parameters are used to study the form of ionospheric scintillations namely,

- $S_4$  index, which is the ratio of standard deviation of changes in signal power to the average ionospheric power.
- $\sigma\text{-phi}$  which is the standard deviation of the phase fluctuations.
- *Decorrelation time* ( $\tau_0$ ), which measures how rapidly phase shifts occur. [17]

The  $S_4$  value can be determined by following equation,

$$S_4^2 = (\langle I^2 \rangle - \langle I \rangle^2) / \langle I \rangle^2 \quad (3.6)$$

where  $I$  is the squared amplitude called signal intensity and  $\langle . \rangle$  represents time average.

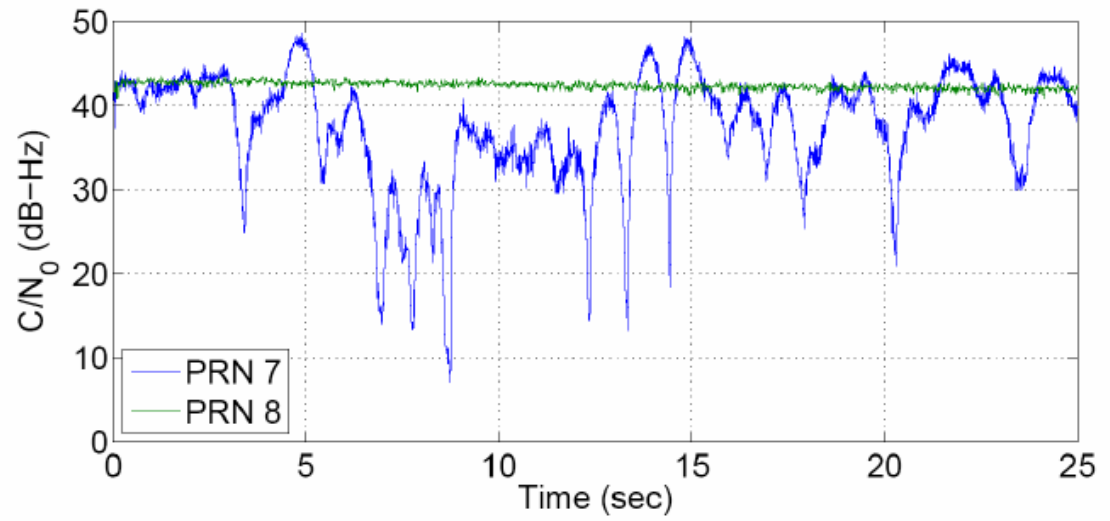


**Figure 3.5:** *The Carrier-to-Noise ratio of scintillating and non-scintillating GPS signal. Reprinted with permission from [17]*

## 4. CHARACTERIZATION OF SEVERE SCINTILLATION EFFECTS ON GNSS

Ionospheric scintillations that affect GNSS system are characterized by different methods. One method is to store the readings of GNSS bandwidth and to feed the recordings into GNSS carrier tracking loops. The problem with this approach is that the recordings are not similar and properties of the recordings varies and are statistically non-stationary [17]. The other method is to alternatively generate scintillation data from first-principles phase screen model [18] and to load the scintillation data into simulator. This approach is not fully developed and severe scintillations are not treated effectively. Therefore, Cornell University selected the option of generating a statistical model and comparing the readings with realtime data observed from GPS receivers and from different wideband satellite systems. The severe equatorial scintillations sets off cycle slipping and sometimes loss of carrier lock. The data simulations that computes the strength of scintillation of phase tracking loops architectures, explains that cycle slips are related to half cycle phase variations and the corresponding power fluctuations. [1] [19]

Scintillations models use *empirical* [20] or *synthetic* [1] amplitude and phase times histories to evaluate the phase variations in GPS simulator output. In Cornell scintillation model, synthetic amplitude and phase time histories are generated artificially using Matlab algorithms and scintillation histories are added to GPS simulator to evaluate phase error variance  $\sigma_{\phi}^2$  and rate of cycle slipping. This thesis focuses on synthetic scintillation datas retrieved from Matlab codes of Cornell scintillation toolbox. However, to understand the concept of gathering scintillation datas, the following section briefly explains the recording procedures of empirical scintillation datas conducted previously by researchers through real-time experiments.

### 4.1 The empirical scintillation library

The Empirical Scintillation Library (ESL) reviews the processes involved in recording of empirical phase and amplitude equatorial scintillations. To study the wide range of strong scintillation effects, equatorial scintillation data were retrieved through two different methods and recorded in empirical scintillation library. The first method is retrieving list of data from a radio beacon experiment, known as DNA (Defence Nuclear Agency) Wideband satellite experiment that was conducted from 1976 to 1979 [21] [22]. A wideband satellite was set-up to transfer 10 signals of consistent continuous

waves from 1000km near-polar orbit. The frequencies of all ten waves were chosen from VHF to S-band in addition to L-band signal at 1239 MHz which is almost coincident with GPS L<sub>2</sub> band signal of frequency 1227.60 MHz. The scintillations disrupted the high frequency S-band signal 2891 MHz in small degree and this was utilized as phase reference for all low frequency signals at the multi-band receiver.

The baseband amplitude and phase outputs from multi-band receiver chain were then converted into digital form at 500 Hz after bandlimiting to 150 Hz. Therefore, [22] the received baseband data were called wideband data. These wideband data were collected at Ancon, Peru (11:8° N latitude) and Kwajaleinatoll, Marshall Islands (9:4° N latitude). These ground stations were installed with 9.1m parabolic tracking antennas and configured with 12-bit quantization and 500 Hz sampling rate. These high gain antennas generated low noise complex signal with high quality. However, whole cycle slips occurred instead of half-cycle slips when receiving the continuous wave signals. Severe scintillation caused whole cycle slips when GPS receiver tracked bi-phase modulated signals and authors emphasized, the absence of half-cycle slips does not reduce the usage of recorded datas.

Of all the signals received by ground stations, the L band 1239 MHz signal is of concern for evaluating the scintillation effects. Severe equatorial scintillation at GPS frequencies diminishes the possibility of test cases conducted with L band signal. To overcome this, UHF carrier data at 447 MHz were added along with L band data to study severe scintillation effects. This suggested that the UHF datas are used for test cases to tackle strong L band scintillation when solar maximum occurs. Ten recorded satellite passes indicating worst scintillation that contains nearly 12 minutes of continuous datas were stored in scintillation library. These passes were recorded as complex time histories with the actual sampling rate of 500 MHz and with no requirement of filtering.

The second method of recording data was done at Cachoeira Paulista, Brazil (22.7° S latitude in December 2003 [23]. These data were containing the collection of GPS L<sub>1</sub> Coarse/Acquisition digital code sampled at 5.7 MHz to be stored in scintillation library. This equatorial region is well known for severe scintillations [24] and it lasted several hours to receive and record data sets from multiple GPS signals that contain worst scintillations. The recorded data sets differed in quality from previous method of recording wideband data, as the datasets from second method are highly processed to filter all the noise and Doppler effects and keep only the scintillation effects. The carrier phase, amplitude and navigation bits were retrieved from the recorded 5.7 MHz samples by processing through software GPS receiver. This method helped eradicate the half-cycle slips from phase time histories, leaving only the whole cycle slips as similar to wideband data. The variations due to effects that include Doppler, receiver clock instability and PLL variations are further processed to remove from carrier phase

output. The output amplitude and phase datas were then sampled at 100Hz to filter noise. The resultant GPS data's SNR was lower than wideband data due to low efficient output of GPS receiver antenna and GPS signal of less strength.

**Table 5.1.** An abstract of empirical scintillation library data. [25]

Data source	Original Carrier Frequency (MHz)	Combined length of records (hours)
Wideband	447 (UHF)	1.9
Wideband	1239( ~GPS L2)	1.9
GPS	1575 (GPS L1)	3.7

To summarize, wideband data are less affected by strong scintillations comparing to GPS L1 data due to the reason that GPS data are scintillated by whole cycle slips. The factors such as low gain antenna and weak strength of GPS signal makes the GPS data's signal-to-noise-ratio to be lower than wideband data. Therefore, GPS data has to be processed more to overcome the above mentioned problems. [25]

## 4.2 Characteristics of strong scintillation

To understand the characteristics of severe scintillation, two distinct samples of scintillation datas retrieved from Cornell scintillation toolbox are considered, one displaying scintillation effects with parameters  $S_4 = 0.9$  and  $\tau_0 = 0.4$  and other with parameters  $S_4 = 0.1$  and  $\tau_0 = 0.04$ . These two samples are shown in Figure 4.1 and Figure 4.2 respectively. These samples exhibit strong scintillation and are denoted by higher scintillation index  $S_4 \approx 0.9$  and lower decorrelation time  $\tau_0 = 0.04$ .

In the figure 4.2, we can see high-frequency ripples of smaller measurements in the plots and this effect proves the fact that, there is rapid phase shifts due to less decorrelation time. The above mentioned effect is independent of similarities existing between both the samples shown in the figures. The common feature found in the severe equatorial scintillation is deep power fades that are visible in upper and lower waves of the plots. The power fades lead to random half-cycle phase changes and the effects are observed in datas recorded in scintillation library. These fades are generally denoted as "canonical fades" and they are the main cause for phase unlock, when PLL tracking of strong scintillation data is carried out. [25]

### 4.2.1 Scintillation severity

Scintillation library data is analyzed using the parameters scintillation index ( $S_4$ ) and decorrelation time ( $\tau_0$ ) and the value of the autocorrelation function of scintillating signal decreases exponentially and decorrelation time denotes the time lag. The scintillation severity can be easily determined for phase tracking by choosing  $S_4$  and  $\tau_0$  values.

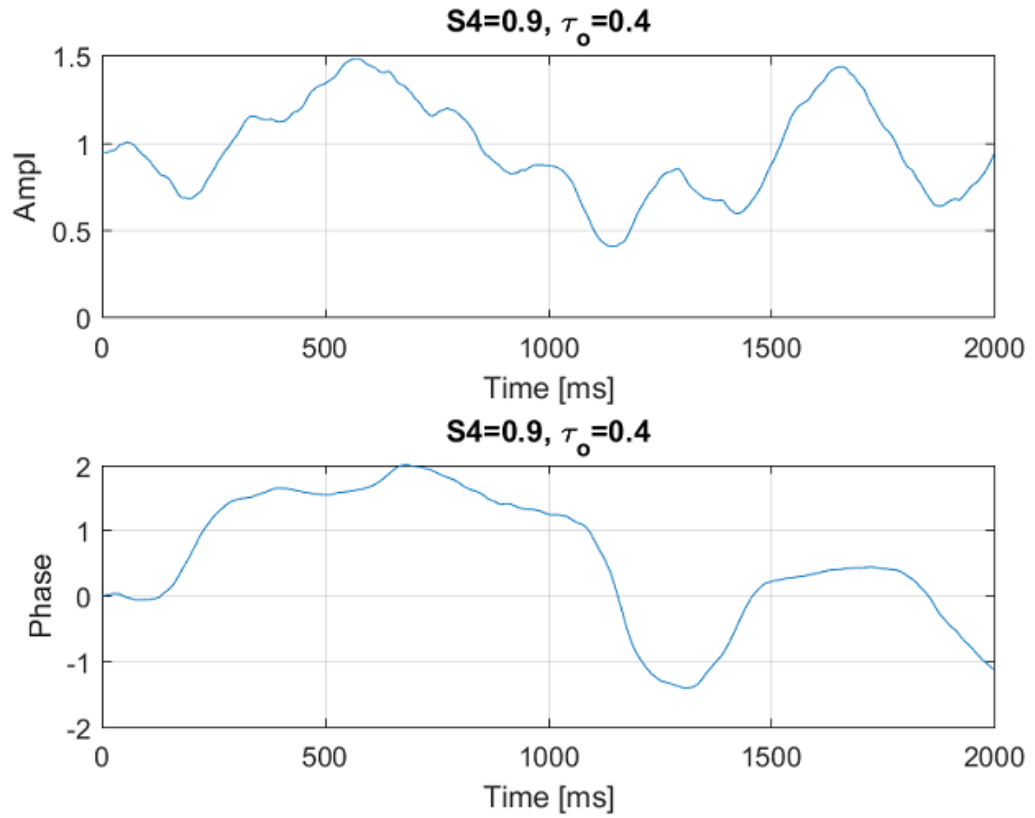


**Figure 4.1:** A sample of Cornell scintillation data showing signal amplitude and carrier phase cycles with  $S_4 \approx 0.9$  and  $\tau_0 \approx 0.4$ .

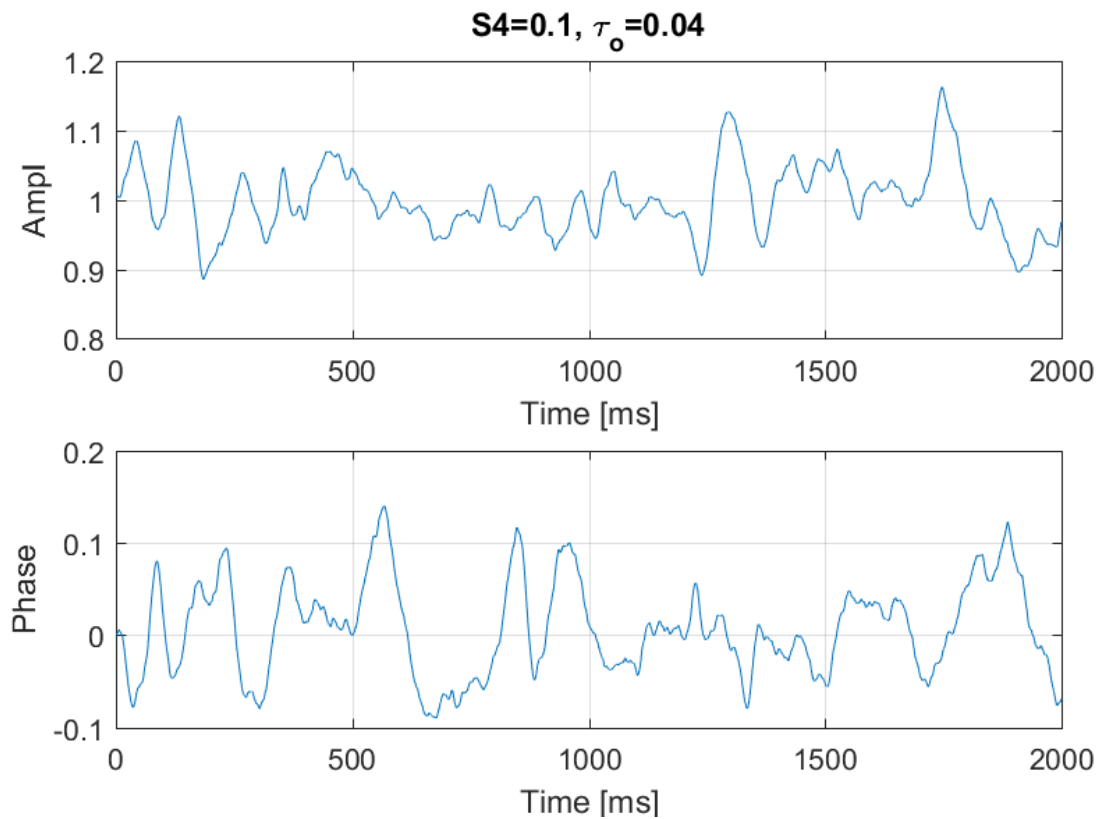


**Figure 4.2:** An other sample of Cornell scintillation data showing signal amplitude and carrier phase cycles with  $S_4 \approx 0.1$  and  $\tau_0 \approx 0.04$ .

If  $S_4$  value is higher or if  $\tau_0$  value is lower then the chosen scintillation intensity is strong. Scintillation library makes it possible by including  $S_4$  value ranging approximately from zero to 1.2 and  $\tau_0$  value ranging from 0 to 2 seconds. When the scintillation ranges from weak to moderate ( $S_4 \leq 0.5$ ), it is apparent that the wideband data selects  $S_4$  indices close to 3.7 times more for the increased frequency 1239 MHz of GPS L-band data. It is approximately scaled by the formula  $S_4 \propto f^{1.5}$  stated by weak scintillation theory [26]. All the scintillation library frequencies saturates approximately to value 1 due to multiple scattering effects, when scintillation severity  $S_4$  is more than 0.5. This shows that UHF scintillation datas are not scintillated severely comparing to strong scintillation datas of wideband L-band and GPS  $L_1$  band.

**Table 4.1.** An example to summarize  $S_4$  and  $\tau_0$  ranges for various scintillation levels. [25]

Scintillation types	$S_4$ ranges	$\tau_0$ ranges (sec)
weak	<0.4	>1.5
moderate	0.4-0.7	0.1-1.5
strong	>0.7	<0.1

The above mentioned result about UHF scintillation is different when observing in terms of decorrelation time ( $\tau_0$ ), as the rapidity of frequencies in UHF band is greater than in L-band data frequencies. This is due to multi-scattering effects that are related to severe scintillation which causes decorrelation time to decrease at lower frequencies [26]. The values of decorrelation time  $\tau_0$ , while recording wideband UHF and L-band datas for storing in scintillation library are recorded as low as 0.12 and 0.4 seconds respectively and this proves that the scintillation severity is higher in UHF band datas. Several ionospheric conditions measures wide range of  $\tau_0$  values while recording scintillation datas from various GPS links. The values are 0.5 seconds for strong scintillation and around 2 seconds for weak to moderate scintillation.

The unexpected fact is minimum  $\tau_0$  values are almost same when scan velocity difference for wideband and GPS L-band data are higher. In addition, the ionospheric F layer (350 km altitude) is the region where strong scintillation occurs due to the presence of irregularities. For figures 4.1 and 4.2, the values of  $\tau_0 \approx 0.4$  and 0.8 and scanning velocities are 4000 m/s and 100 m/s and background ionospheric drifting velocities are from 100 to 200 m/s respectively for wideband and GPS L-band. The higher difference in scanning velocities of GPS L-band and wide band does not affect the  $\tau_0$  values. This is due to the geometry behind ionospheric structures and relative velocity of drift rate to scan velocity vector. [17]

Therefore, wideband UHF data were used [25] as an alternative to GPS L<sub>2</sub> data for studying and testing GPS tracking loops. When S<sub>4</sub> increases and τ<sub>0</sub> decreases, scintillation data are not easy to track and so larger τ<sub>0</sub> value in wideband UHF data are capable of tracking GPS signals. Increased S<sub>4</sub> and τ<sub>0</sub> values have disadvantage of deep power fades exceeding 15 dB and exist for more than 2 seconds. This is applicable for static receivers and for dynamic receivers deep power fades lasts longer than 2 seconds. Scintillation libraries store such long lasting scintillation datas by modifying library's sampling interval. [17] [25]

#### 4.2.2 Power phase spectra and first-order statistics

Scintillation modelling involves other statistical parameters that are plotted in figures 4.3 and 4.4, respectively. Figures 4.3 (b) and 4.3 (c) shows the plot of empirical first-order phase rate and amplitude distributions. Figure 4.3 (a) shows the empirical joint distribution of full 5 minutes sample GPS record by plotting phase change Δθ in 20ms interval per bit over the normalized fading amplitude α. The distribution of the severely scintillating data shows the canonical fading effects as the value of phase change Δθ distribution is widespread when amplitude α value is smaller. The phase errors also contribute in minimal effects to some of the spreading in Δθ. First-order amplitude distribution in figure 4.3 (c) is consistent with the Rice distribution [27] and more concurrent with well known Nakagami-m distribution [28], and is expressed by,

$$p(\alpha) = [2m^m \alpha^{2m-1} / \Omega^m \Gamma(m)] (e^{-m\alpha^2/\Omega}) \quad (4.1)$$

where m is the shape parameter determined by 1/S<sub>4</sub><sup>2</sup> and Ω is spread value identical to E[α<sup>2</sup>] which is mean-square of fading amplitude and is normalized to 1 and Γ(m) is gamma function of m. In realtime, expected values E[.] are estimated approximately as time average ⟨.⟩ over stationary time intervals. Occurrence of cycle slipping caused by scintillation is evident from the long tail in figure 4.3 (b) from probability distribution of phase change Δθ.

Scintillation effects modeling of various data samples are characterized by another approach called power phase spectrum, shown in figure 5.4. To display wide range of frequencies, GPS L<sub>1</sub> data is utilized without filtering. For phase tracking, all the three spectra in figure 4.4 are obtained from severe scintillating data, with S<sub>4</sub> value chosen above 0.9. Spectra values are approximated and plotted by power law stated by weak-scatter phase screen theory [18] given by,

$$S_{\theta}(f) = T / (f_0^2 + f^2)^{p/2} \quad (4.2)$$

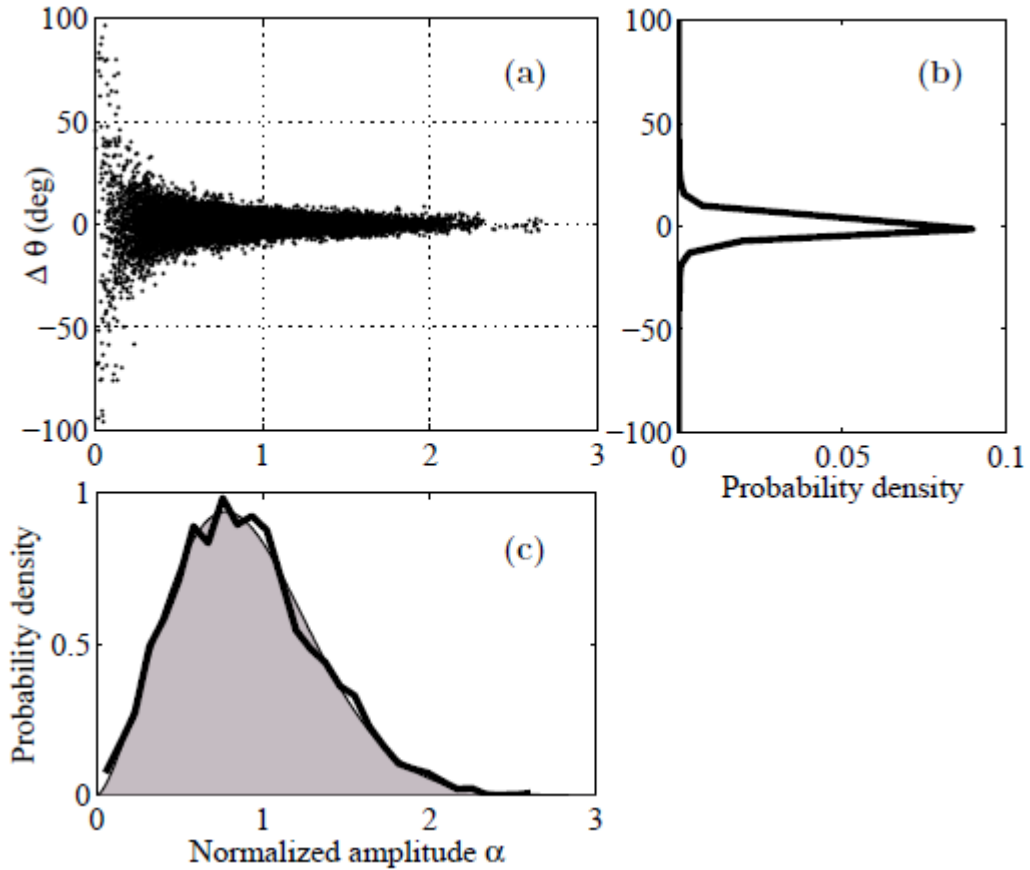


**Figure 4.3:** (a) Empirical joint distribution (in density of samples) of the variables  $\Delta\theta$  and  $\alpha$ . (b) Empirical first-order phase rate distribution in  $\Delta\theta$ . (c) Empirical first-order amplitude distribution in  $\alpha$  (thick black line) consistent with the Nakagami- $m$  distribution (greyed area) corresponding to the empirical  $S_4$  value. Reprinted with permission from [25] [28]

where  $p$  is the phase power law index,  $T$  is the strength parameter,  $f_0$  is the temporal frequency of ionospheric outer scale and it is not considered practically as the value is much smaller than the frequencies of interest and irrelevant to cause PLL phase errors and negligible PLL noise bandwidth of approximately 10 Hz. Therefore, the power law equation is approximated to  $S_\theta(f) = T f^p$ , where  $T$  is power density at 1 Hz. The curve at GPS  $L_1$  data spectra at 10 Hz frequency indicates the noise floor and this effect is not available in wide band data upto Nyquist cutoff frequency 250-Hz. When testing, wide band library records are modeled as containing no noise components and GPS data records are modeled as having familiar noise component that cannot be lowered.

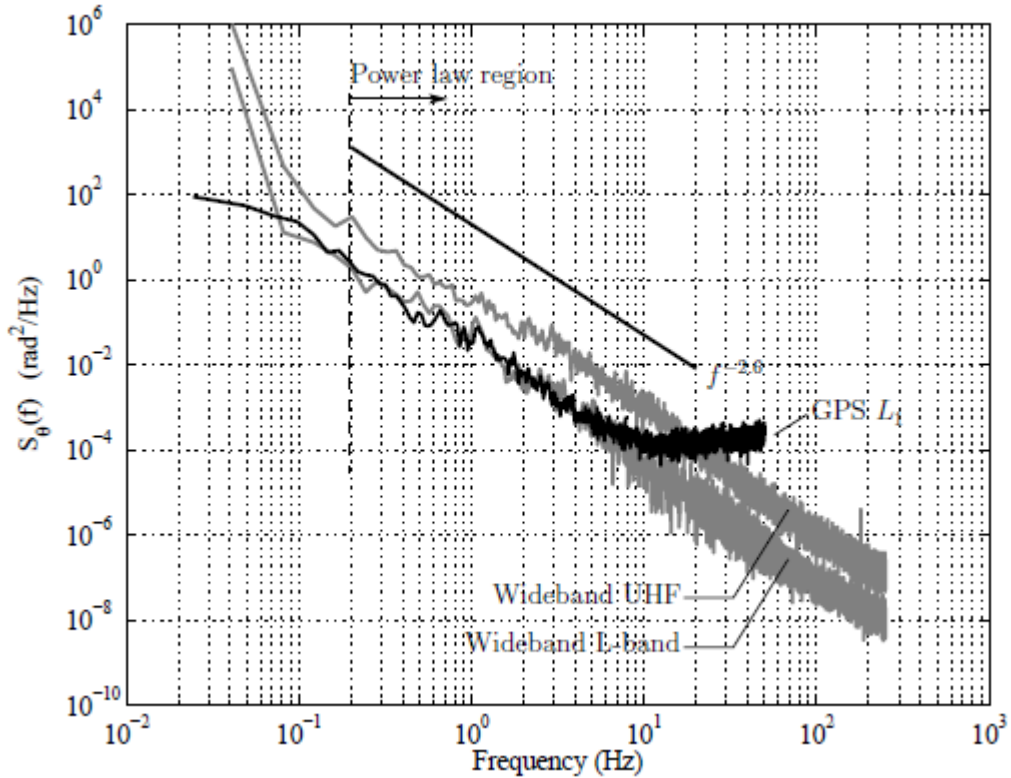


**Figure 4.4:** Phase power spectra of data samples of GPS  $L_1$ , Wideband L-band and Wideband UHF. The solid black line displays reference spectral slope relative to  $p = 2.6$ . Reprinted with permission from [25] [18]

A review of all library records shows same value of  $p = 2.6$ , an empirical limit for scintillation severity  $S_4$  more than 0.9. This limit reduces towards 2 when GPS data spectra reaches noise floor. The reducing effect is due to rapid, discontinuous and large phase changes caused by canonical fading. Phase scintillation is not bounded to any specific frequency and so the power phase density occasionally cross the PLL tracking bandwidth causing phase tracking errors which in turn results in cycle slips. [25]

### 4.2.3 Canonical fading

Canonical fading is an important effect to be analysed in order to conduct scintillation tests though this thesis work does not include this effect. Canonical fading are deep power fades that occurs due to rapid phase shifts during strong scintillation. This sudden change in phase introduces amplitude fluctuations that affect the carrier phase tracking. The phase measurement would be difficult when fading lowers SNR value, also called low loop SNR. This results in cycle slips at around 1150ms and 1220ms from Figures 4.1 and 4.2 respectively. The quick changes in phase causes phase errors due to low value of SNR. Nevertheless, it is found from the scintillation data figure 4.2, that the total phase change is reduced if the required SNR is maintained as against the scintillation data in figure 4.1, which shows high frequency ripples lowering SNR value. One can easily understand the canonical fading phenomenon by

representing complex baseband signal on complex plane shown in Figure 4.5, reprinted with permission from [25]. The speed of phase and amplitude of the signal moving on the plane is inversely proportional to the value of  $\tau_0$  and the phasor magnitude wandering more near the origin in the figure 4.5, shows half cycle phase shifts, responsible for canonical fading.

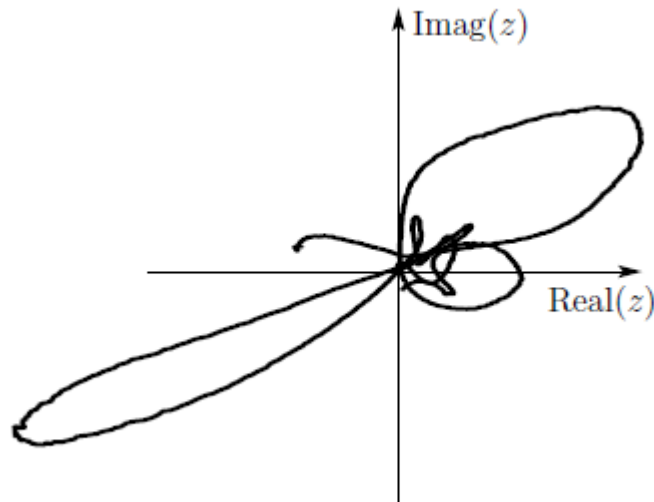


**Figure 4.5:** *An example of planar representation of complex baseband signal  $z(t)$  showing canonical fading near origin due to half cycle phase shifts. Reprinted with permission from [25]*

### 4.3 Scintillation effects on Acquisition

This chapter briefs the methods of acquisition on GPS receiver and effects of scintillation on detection performance in terms of detection probability ( $P_d$ ). Various acquisition methods assist in improving detection performance using coherent and non-coherent integrations [29]. The methods include, for example data folding method, serial search method, repetitive block acquisition method, zero padding method and FFT based circular correlation method [30]. The next section explains FFT based circular correlation method, which is frequently used in GNSS receivers due to its improved detection performance [31].

#### 4.3.1 Parallel FFT based circular correlation

FFT based circular correlation method uses the search strategy that estimates two parameters, code frequency and code phase. Code frequency is the signal frequency value acquired by receiver whereas code phase denotes the point at which PRN code of the satellite starts during acquisition. The block diagram of FFT based circular correlation is shown in Figure 4.6. [30]

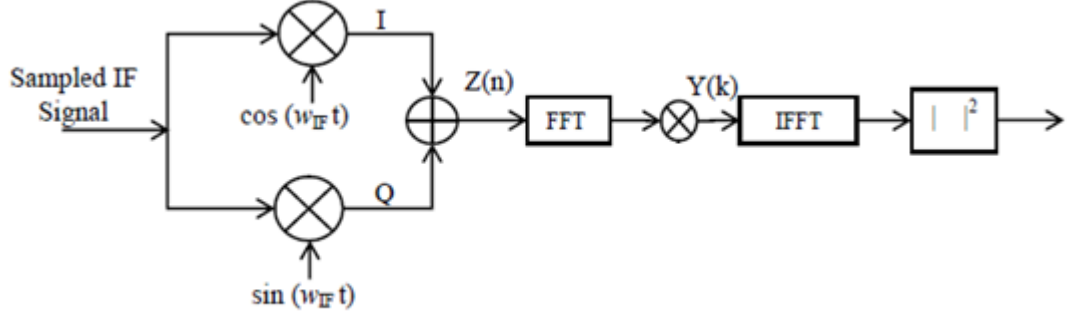


**Figure 4.6:** A simple block diagram of Parallel FFT based circular correlation

The received GNSS signal is shown in the following equation given below,

$$s(t) = A d_r(t) c_r(t) * \cos(2\pi(f_L + f_d)t + \theta) + n(t) \quad (4.3)$$

where  $A$  denotes signal amplitude,  $d_r(t)$  is data bit,  $c_r(t)$  is the GNSS reference code and  $f_L$  is carrier frequency of L-band GNSS signal,  $f_d$  is unidentified Doppler shift value,  $\tau$  is unknown phase error value and  $\theta$  and  $n(t)$  are phase and noise of the received signal respectively. The downconversion to IF signal is performed by mixing the received signal with local oscillator signal and result of sampled IF signal is given by,

$$s_{IF}[n] = A d_r[n] c_r[n] * \cos(2\pi(f_{IF} + f_d)nT_s + \Delta\theta) + n_{IF}[n] \quad (4.4)$$

where  $T_s$  is sampling time interval,  $f_{IF}$  is frequency of downconverted signal,  $\Delta\theta$  is phase difference between received signal and reference oscillator signal and  $n$  is total number of signal samples. The IF signal is correlated with locally generated GNSS code by passing through acquisition algorithm performed using FFT based circular correlation method. This is done by multiplying IF signal with reference sine and cosine signals in order to eliminate carrier components, thereby resulting in-phase and quadrature components given by,

$$s_I = A d_r[n] c_r[n] * \cos(2\pi f_d n T_s + \varphi) + n_I[n] \quad (4.5)$$

$$s_Q = A d_r[n] c_r[n] * \cos(2\pi f_d n T_s + \varphi) + n_Q[n] \quad (4.6)$$

where  $n_I[n]$  and  $n_Q[n]$  are in-phase and quadrature noise components and considered as Gaussian white noise with zero mean and variance  $\sigma^2$  ( $n_I[n], n_Q[n] \sim N(0, \sigma^2)$ ). The in-phase and quadrature components are added to form complex signal ( $z(n)$ ) and converted to frequency domain using FFT. The circular correlation is performed by multiplying  $z(n)$  with conjugate FFT of GNSS coded signal generated locally. The result is then converted into time domain using IFFT and then absolute value of result is

taken to end the correlation process. The signal is present and satellite is found to be detected when a peak is found exceeding certain threshold. [30]

### 4.3.2 Detection probability and performance

The in-phase and quadrature components of the incoming signal and locally generated GNSS coded signal is given as,

$$I = A' d_{\tau}[n] R(\theta') * \text{sinc}((f_d - f_{d'})T_I \cos\theta_i) + n_{Ii} \quad (4.7)$$

$$Q = A' d_{\tau}[n] R(\theta') * \text{sinc}((f_d - f_{d'})T_I \sin\theta_i) + n_{Qi} \quad (4.8)$$

where  $R(\theta')$  is autocorrelation function,  $\theta' = \tau - \tau'$  is correlation loss by code delay.  $f_d - f_{d'}$  is Doppler offset,  $\theta_i$  is average phase error during correlation time interval and  $T_I$  is coherent integration time. If the signal is considered to contain strong amplitude variations due to scintillation, and affected signal contains affected amplitude  $A'$ , then the relation is given as  $A_N = A'/A$ , where  $A_N$  is normalized signal amplitude  $A$  is unaffected signal amplitude. Therefore, detection probability is dependent on amplitude and PDF of the signal in terms of amplitude is given by,

$$P_{HI}(E) = P_{HI,A'}(E|A')P_{A'}(A)dA \quad (4.9)$$

where  $P_{A'}(A)$  is degradation of detection probability due to the presence of amplitude scintillation and can be represented as Nakagami-m distribution [32]. Therefore, detection probability with amplitude scintillation is given as,

$$Pd = \int_0^{\infty} P_{HI,A'}(E|A')P_{A'}(A)dA \quad (4.10)$$

The value of detection probability is decreased when scintillation intensity  $S_4$  is higher. To enhance detection probability of signal, two approaches, namely coherent and non-coherent integrations, are carried out during acquisition stage. For example, if we use 1 ms signal for signal acquisition, the input  $S/N_0$  of 14 dB is reasonable value for 90 % of detection probability [33]. The coherent integration gain of data over 'n' ms,  $G_c(n) = 10\log(n)$ . Coherent integration is practically possible upto the length of navigation data bit, in order to avoid integration over the bit transition. In Galileo open service signals, the data bit length is 4 ms. For weak signals, acquisition is done by the combination of coherent and non-coherent integrations. The non-coherent integration gain is given by  $G_i(n) = G_c(n) - L(n)$  where  $L(n)$  is non-coherent integration loss.

Performing multiple non-coherent integrations increases the gain, for instance to achieve 14 dB gain with 90 % detection probability, 100 non-coherent integrations are done for 1 second of data according to the studies in [34]. Another instance found in

[35] shows that 4 seconds of data were processed to receive 26 dB gain at the output. If achieved gain is negligible then the number of non-coherent integrations is reduced in order to limit additional operations.

#### 4.4 Scintillation effects on code tracking loops

In paper [38], an example simulation results were done to evaluate the receiver signal tracking performance. The scintillation effects were studied based on the variance of code tracking loop errors using tracking models in [37]. The methods in the model were used to characterize receiver tracking performance of Galileo E1 signal during weak to strong scintillations. The receiver input data includes, amplitude and phase scintillation indices ( $S_4$  and  $\sigma_\phi$  respectively), and spectral parameters namely, the spectral slope  $p$ , and spectral strength  $T$ . The variance of the tracking error is evaluated at the output of the code tracking loops using tracking models that analyse scintillation effects. The scintillation histories are retrieved from Cornell scintillation model with different scintillation intensities of  $S_4$  values, 0.5, 0.6 and 0.7 along with constant  $\tau_0$  value of 0.5s. This generated the scintillation time histories of 30 minutes length. Appropriate DLL bandwidths were chosen for the three simulations, for instance 0.25 or 0.1 Hz.

The simulator Spirent GSS8000 GNSS is used to track the affected Galileo E1 signal. The degradation of the receiver performance during different levels of scintillations were analysed by estimating variance at the output of the delay-locked loop for code tracking loops. The simulation result of increasing phase tracking error is shown in terms of variance [37] [36]. Scintillation data were simulated for total of 15 minutes and the variance was measured as 0.04 radians with PLL linearity at 11<sup>th</sup> minute of the simulation. The effect of strong scintillation increased the variance to the peak value of 0.14 radians at 12<sup>th</sup> minute which showed the increased carrier phase tracking error during strong scintillation. Figure 7.10, from the simulation result of this thesis, shows the example plot of degradation of receiver performance in terms of RMSE, retrieved from TUT MBOC simulator, with  $S_4$  levels, 0.9, 0.4 and 0.15. The plot also shows the better performance of AWGN signal comparing to scintillated signal.

## 5. CORNELL SCINTILLATION MODEL

A simple model was developed by Cornell University to simulate ionosphere induced scintillation that tests and identifies the properties that affect phase tracking loops. This model works as scintillation simulator with two inputs: the scintillation index  $S_4$  and the decorrelation time  $\tau_0$ . This model also assumes Rice distribution for scintillation amplitude and the spectrum of highly varying complex component of scintillation is considered to follow 2<sup>nd</sup> order low-pass butterworth filter [43]. The expectation of solar maximum in the year 2011, lead to greater interest in testing GPS receivers of strong scintillation effects. One way of testing receiver is to retrieve scintillation time histories from empirical library of scintillation records. The strong scintillation data record includes effects such as deep power fades of more than 15 dB, and the half cycle phase transitions. These canonical fades are the main cause of loss of lock in GPS carrier tracking phase loops. [44]

The study of scintillation effects using realistic empirical data histories has various disadvantages. Firstly, the researchers have limitations to adjust the output only to some degree as the behavior is stored in the recorded data sets. Secondly, thermal noise recorded in receiver produces high frequency deviations and this limits the specification of carrier to noise ratio of a scintillation testing [44]. Extended testing is not possible using empirical scintillation data records for the reason that the empirical data records statistically represent stationary output for short interval of time. The statistical model output of the scintillation data are made realistic such that the shape of amplitude and phase spectra are plotted independently [45]. This is carried out by artificially tracking carrier phase with minimal canonical fades and this in turn helps in properly shaping the complex scintillation data. The following section explains the scintillation model that analyses complex equatorial scintillation as it is known for tracking difficulties. This model analyses scintillation datas through amplitude distributions and power spectra and the effects of model are validated by comparing it with phase screen generated models. [43]

### 5.1 Scintillation model

The model used here works on the conception that the scintillation induced cycle slips occurs during phase tracking and also the scintillation properties cause bit errors in 250 bps binary navigation message of phase modulated L-band Galileo signal [44]. The rapid phase changes between data bits (4 ms long) due to noise and scintillation, limits

one from accurately concluding if the bit change occurred, thus there is low probability to know the occurrence of cycle slips. The mean time between cycle slips  $T_s$  and mean time between bit errors  $T_e$  of phase tracking loops provides good scintillation performance when the parameters works in a relation  $T_s/2 < T_e \leq T_s$ . Here  $T_e$  can be approximated to  $T_s$  such that problematic cycle slip prediction is made easier through predictable bit error problem.

To determine  $T_e$  for complex scintillation signal, one require complex channel response function  $z(t)$  also considered as scintillation time history whose phase and magnitude changes are the effect of scintillating communicating channel on GNSS carrier signal. One can artificially synthesize scintillation when  $z(t)$  correctly tracts  $T_e$  due to close relation between  $T_s$  and  $T_e$ . This is possible because the model tracks the scintillation properties that are responsible for cycle slips and this assumption is validated later in the validation section. Estimation of  $T_e$  is based on two properties of  $z(t)$ , *amplitude distribution*  $p(\alpha)$  and the *measure of rapidity* of which  $z(t)$  wanders about the complex plane [44]. Let's assume normalized  $z(t)$  such that  $\Omega \equiv E[\alpha^2(t)] = 1$ , where  $\alpha(t) = |z(t)|$ , and the value of  $z(t) = 1$  when no scintillation.

The fast transitions of  $z(t)$  nearby origin causes rapid phase shifts in  $z(t)$  and this at its turn causes changes in adjacent data bits. Thus one can predict  $T_e$  from the facts such as the probability of the response close to origin  $p(\alpha)$  and the speed of  $z(t)$ . To determine  $T_e$ ,  $z(t)$  is considered to be in the form,

$$z(t) = z + \xi(t) \quad (5.1)$$

where  $z$  represents complex direct signal considered to be independent of time and  $\xi(t)$  is the complex varying multipath component that represents scattered signals in the ionosphere. In other words  $\xi(t)$  is denoted as fading process and its autocorrelation is given by,

$$R_\xi(t) = \frac{1}{2} E[\xi^*(t) \xi(t + \tau)] \quad (5.2)$$

The decorrelation time  $\tau_0 > 0$  is related to cutoff frequency with the time  $\tau$  at which  $R_\xi(t) / R_\xi(0) = e^{-1}$ , an exponential function. When  $\tau_0$  is small, shape of  $R_\xi(t)$  is narrow because of small width of main peak. This indicates the scintillation channel that changes severely with time and also helps us find the speed of  $z(t)$  near origin. Therefore, this scintillation model is further elaborated in the following section with detailed specifications of  $p(\alpha)$  and  $R_\xi(t)$ .

### 5.1.1 Amplitude distributions

The probability distribution of  $z(t)$  is not predictable and there are no theories to predict it without limitations. Though there exist few theories that characterize first order

distribution [26] [21], when scintillation severity reaches the saturation point amplitude distribution  $p(\alpha)$  is approximated to Rayleigh distribution. However, this is applicable for empirical or numerical datas to predict the distribution of  $z(t)$ . The number of distributions of  $z(t)$  were determined for scintillation datas from wideband satellite experiments [21]. The test results showed that the Nakagami-m distribution was the suitable approach for evaluating amplitude distributions. This result is not conclusive for UHF and nearby frequencies as the datasets lasted for 20 seconds and less availability, 20 datasets at UHF and 9 sets at L-band. In addition, time correlation in empirical  $z(t)$  is not crystal clear in this analysis.

This analysis of Cornell scintillation model serves as a suitable model for amplitude distribution that concentrates on severe scintillation at frequencies UHF and L-band and the model approaches Nakagami-m and Nakagami-n (Ricean) distributions [27],

$$p_m(\alpha) = [2m^m \alpha^{2m-1} / \Omega^m \Gamma(m)] (e^{-m\alpha^2/\Omega}) \quad (5.3)$$

$$p_n(\alpha) = [2\alpha(1 + K) / \Omega] * (I_0) * 2\alpha * (\sqrt{[(K + K^2) / \Omega]}) * (e^{-K-(1+K)\alpha^2/\Omega}) \quad (5.4)$$

where  $K$  is Ricean parameter,  $\Gamma(\cdot)$  is the gamma function,  $\alpha \geq 0$  and  $m = 1/S_4^2$  and  $S_4$  is standard scintillation index. The relation between Ricean parameter  $K$  and  $m$  is given by,

$$K = \sqrt{m^2 - m} / (m - \sqrt{m^2 - m}) \quad (5.5)$$

Both Nakagami-m and Rice distributions have similar properties to Rayleigh distribution when  $S_4 = m = 1$ . When scintillation severity is high, i.e.,  $S_4 > 1$ , Nakagami-m distribution is defined, but not the Rice distribution. At  $S_4 < 1$ , Nakagami-m and Rice distributions are same in properties and both the distributions are close to data representation of wideband UHF scintillation data from empirical library as shown in Figure 5.1. This figure is altered version of the phase screen model presented in figure 4.3c that displays amplitude distribution of scintillation data. This is done by modifying single phase screen with two phase screens with distance of 100km. The phase screen model was validated and accepted by researchers and scientists [18].

The phase screen model calculates the phase fluctuations or scintillations using single or multiple layers. Each layer is described as phase screen and for multiple layers, for instance, two phase screen model, phase synthesis is performed successively for both the layers perpendicular to the direction of propagation. The synthesized phase data fluctuations are used as scintillation data to study [46]. Therefore, the phase screen data is the scintillation data generated by phase screen model. This paper uses the phase screen model as an aid for phase spectrum analysis in Cornell scintillation model. The

only drawback of phase screen model is when scintillation severity  $S_4$  is between 0.6 and 1, the amplitude distribution of phase screen model depart away from the amplitude distributions of empirical scintillation data. When carrier tracking is performed, this drawback acts as one of the reasons to develop statistical scintillation model over phase screen model.

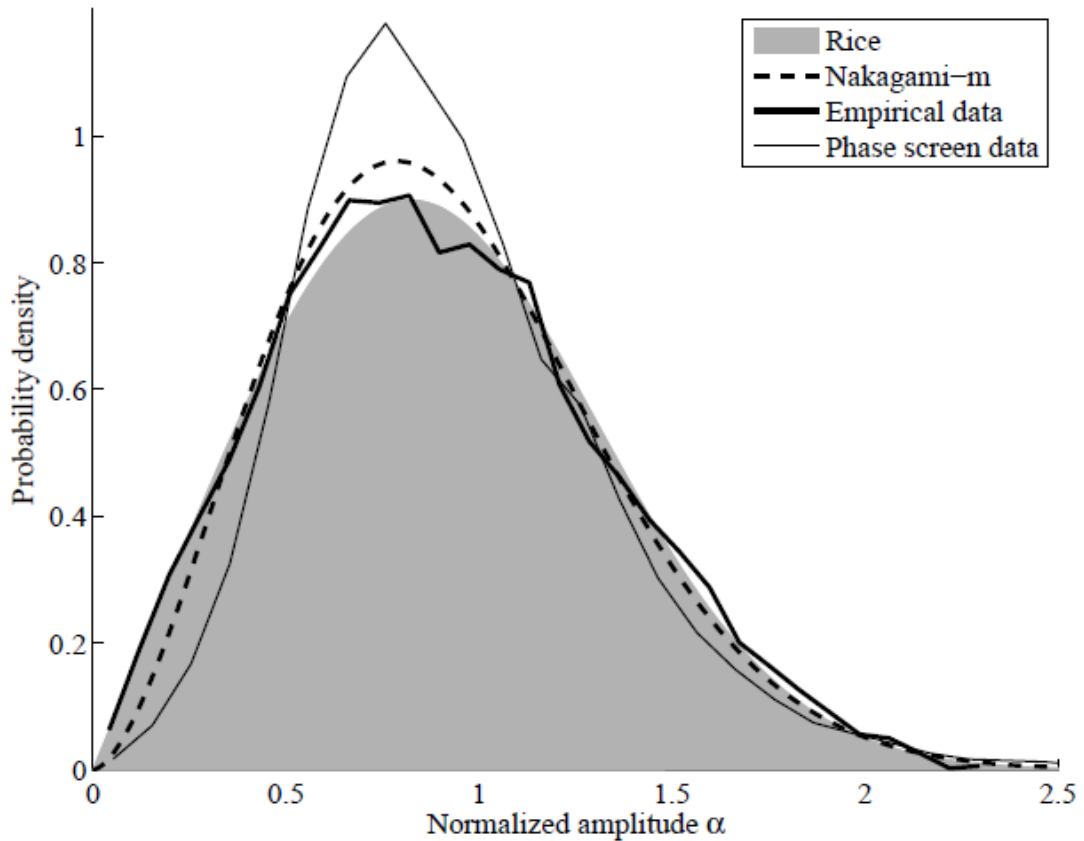


**Figure 5.1:** Nakagami- $m$  and Rice distributions in comparison with amplitude distribution of wideband data from empirical scintillation library and also with amplitude distribution of scintillation data generated by phase screen model. The value of  $S_4$  is 0.87 for all the above distributions. Reprinted with permission from [43].

Average chi-square values were estimated for the scintillation datasets retrieved from scintillation library to determine the correctness of amplitude distributions of Nakagami- $m$  and Rice distributions [25]. The calculations were done for scintillation library records of 79 sets of wideband UHF data and 33 sets of GPS L1. The data records were inspected properly and stationary interval of length ranges from 50 to 300 seconds are chosen that corresponds to strong scintillation  $S_4 > 0.6$ . In chi-square calculations, time interval between data samples are twice the decorrelation time of the total interval. This is to make sure that the data samples are independent and the length of each dataset is chosen to work with 100 samples. Therefore, decorrelation time  $\tau_0$  is

long and so the longer datasets were chosen to generate 100 independent data samples. On calculating chi-square statistic, the datasets were partitioned to number of bins known as chi-square Degree of Freedom (DOF) [43]. Here, eight chi-square DOF for the Wideband UHF data and seven chi-square DOF were used.

The chi-square test results are shown in the table 5.1 and chi-square DOF for both Nakagami-m and Rice distributions are almost in close proximity for the number of sets (a-dimensional). This proves that the Nakagami-m and Ricean distributions serve as a suitable option for scintillation data with Rice distribution having additional benefits for both data sources, wideband UHF data and L1 datasets.

**Table 5.1.** Chi-square values for Nakagami-m and Rice distributions [43]

Data source	No. of Sets	Nakagami-m(DOF)	Rice(DOF)
Wideband UHF	79, 8	11.8 +/- 8.8	9.0 +/- 4.3
GPS L1	33, 7	8.42 +/- 5.9	7.7 +/- 5.7

The reason for choosing Rice distribution is its easier implementations in practical environment with the assumption that the fading process is Gaussian and the value of amplitude of Rice distribution results in  $\alpha(t) = |z(t)|$ . Therefore, in Cornell scintillation model, it is assumed that the fading process  $\xi(t)$  to be Gaussian random process with autocorrelation time and complex, stationary and zero mean.

### 5.1.2 Autocorrelation function of the scintillation model

The autocorrelation function  $R_{\xi}(t)$  has to be defined in order to complete scintillation model. Along with this, the power spectrum  $S_{\xi}(f)$  of the fading process  $\xi(t)$  is defined and the power spectrum is associated with  $R_{\xi}(t)$  through Fourier transform. Modeling the scintillation effects make the equation  $z(t) = z' + \xi(t)$  to be sufficient, but the results do not include low frequency components during scintillation. The previous scintillation studies ensure the complex scintillation signal to be considered completely. For instance, in weak scintillation, the power spectra includes the amplitude,  $\alpha(t) = |z(t)|$  and intensity  $I(t) = \alpha^2(t)$ , whereas for severe scintillation, the value of direct component  $z'$  is too small to be considered and fading process  $\xi(t)$  will be equal to  $z(t)$ . Therefore, strong scintillation limits the correctness of scintillation theory [26] and practical experiments are taken into account to define power spectrum  $S_{\xi}(f)$ .

To specify the power spectrum  $S_{\xi}(f)$  in relation to time histories of empirical and phase-screen generated scintillation, high pass filter is used to remove low frequency components of phase time history. Here only phase of  $z(t)$  is changed using filter and spectra of amplitude and intensity are not altered. During the process, the cutoff frequency of filter is adjusted and filtered to derive equivalent mean and variances of quadrature components of  $\xi_f(t) = z_f(t) - z'$ . Here base 'f' indicates the filtered components. The filtered version and the original scintillation time histories are found

to have equivalent effect for carrier tracking loops. This was proved by simulating both  $z(t)$  and  $z_f(t)$  using software tracking loops [44] and observing equal performance of loops.

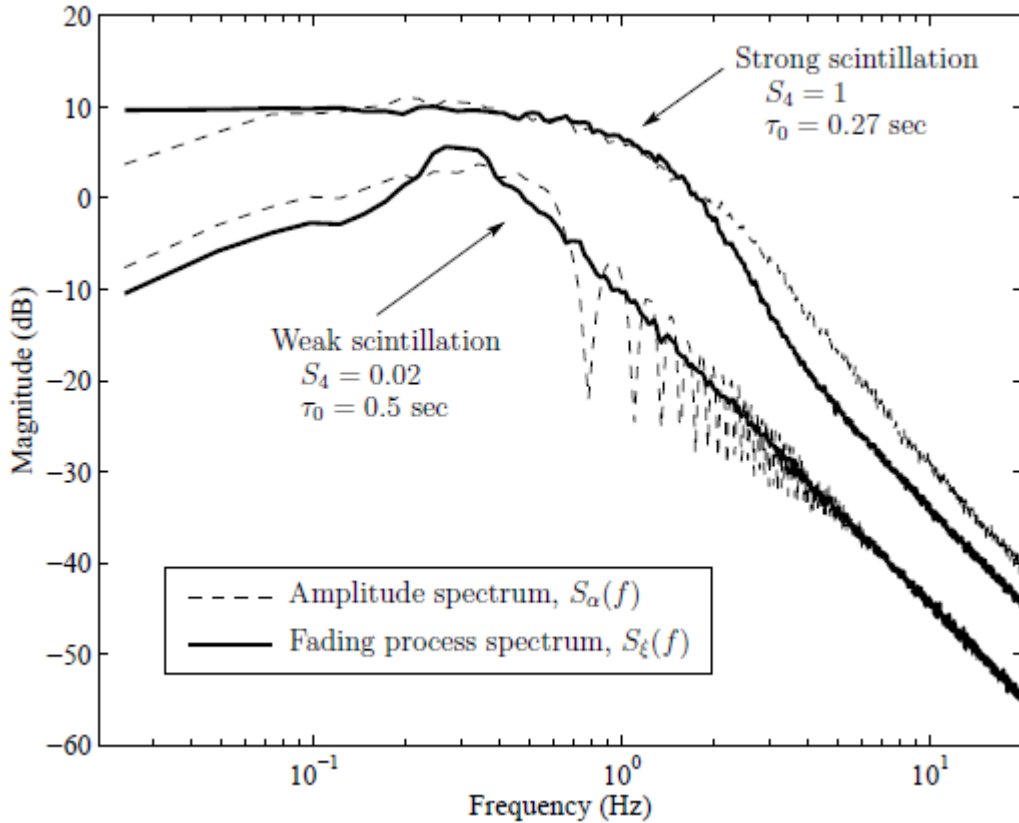


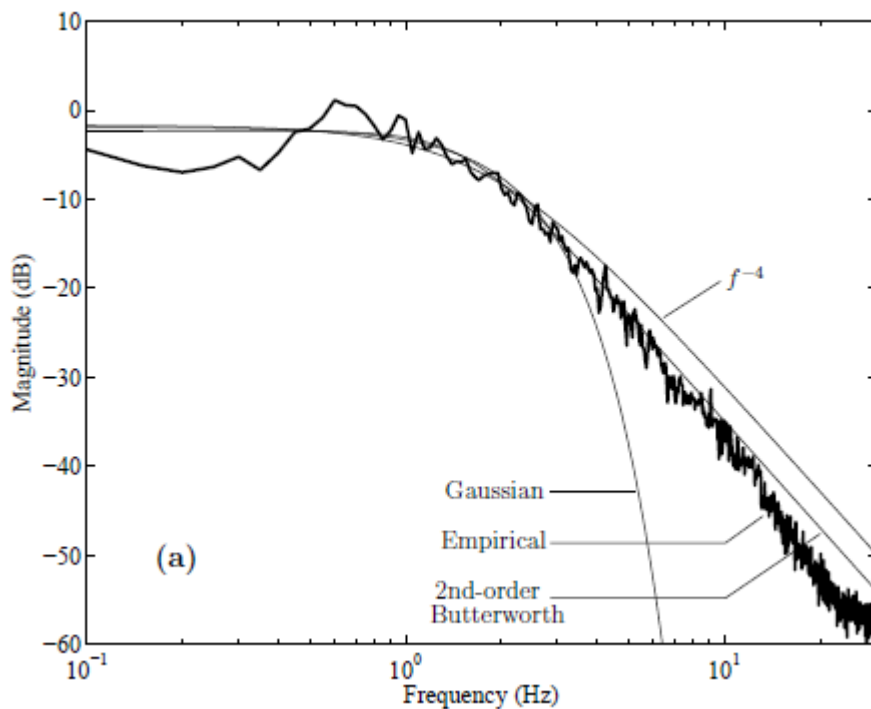
**Figure 5.2:** Comparison of power spectra of amplitude and fading process in the weak and strong scintillation time period corresponding to phase-screen generated scintillation data. For visual clarity, weak and strong scintillation spectra are purposely offset from each other by 10 dB. Reprinted from permission from [43]

The filtering technique mentioned above satisfied the specifications of both empirical and phase screen generated scintillation time histories. The power spectrum  $S_{\xi}(f)$  of filtered time histories can obviously be specified and figure 5.2 shows the same for phase-screen generated model plotting both weak and strong scintillation time histories. Weak scintillation case uses single phase screen with low perturbation strength of  $C_s = 10^{19}$  [47] and for strong scintillation two phase screens with high perturbation strength of  $C_s = 10^{22}$  was used. Figure 5.2 also displays amplitude spectrum  $S_{\alpha}(f)$  for both weak and strong cases. Weak scintillation amplitude spectrum is concurrent with weak scintillation theory model [48]. At low frequencies, amplitude spectrum is uniform till the break point called Fresnel frequency,  $f_F$ . Fresnel oscillations are formed after breakpoint and rolls toward high frequency asymptote. At strong scintillation amplitude spectrum, Fresnel frequency is not clear as the spectrum is broader, though the spectrum reaches high frequency asymptote.

The important point to be noted in figure 5.2 is that the shape of the fading spectrum  $S_{\xi}(f)$  agrees closely to the shape of amplitude spectrum  $S_{\alpha}(f)$  for strong scintillation. This is evident from the empirical findings [49] of strong scintillation (approximately  $\xi(t) = z(t)$ ) where amplitude distortions are the main reason for shape formation of quadrature components of  $z(t)$ . Therefore, the plots in figure 5.2 propose the fading spectrum of low-pass filter with a 2<sup>nd</sup>-order rolloff. Hence, Cornell scintillation model uses 2<sup>nd</sup> order Butterworth filter to be modelled for fading spectrum  $S_{\xi}(f)$ . In this case, the autocorrelation function  $R_{\xi}(\tau)$  is defined by [50],

$$R_{\xi}(\tau) = \sigma_{\xi}^2 e^{(-\beta|\tau|/\tau_0)} [\cos(\beta\tau/\tau_0) + \sin(\beta|\tau|/\tau_0)]$$

Where  $\beta = 1.2396464$  and the model is displayed in two forms for scintillation spectra namely, Gaussian and  $f^{-4}$  [51]. Figure 5.3(a) shows the empirical fading process spectrum  $S_{\xi}(f)$  from scintillation library of  $S_4 = 0.87$  and compared with the models Gaussian and  $f^{-4}$  and 2<sup>nd</sup> order butterworth filter provided all the models are matched to the decorrelation time  $\tau_0$  of empirical scintillation data. Autocorrelation functions normalized to  $R_{\xi}(\tau) / R_{\xi}(0)$  corresponding to the spectra in figure 5.3 (a) are shown in figure 5.3(b). The inset of figure 5.3 (b) shows the bit by bit variations of  $z(t)$  and it displays first 40 ms of the autocorrelation plots. Therefore, amplitude distribution and autocorrelation shape of first 40 ms defines the probability of error in binary bit detection in the proposed scintillation model. To conclude, from the above factors 2<sup>nd</sup> order Butterworth filter is easier to implement and chosen as the best option for Cornell scintillation model.



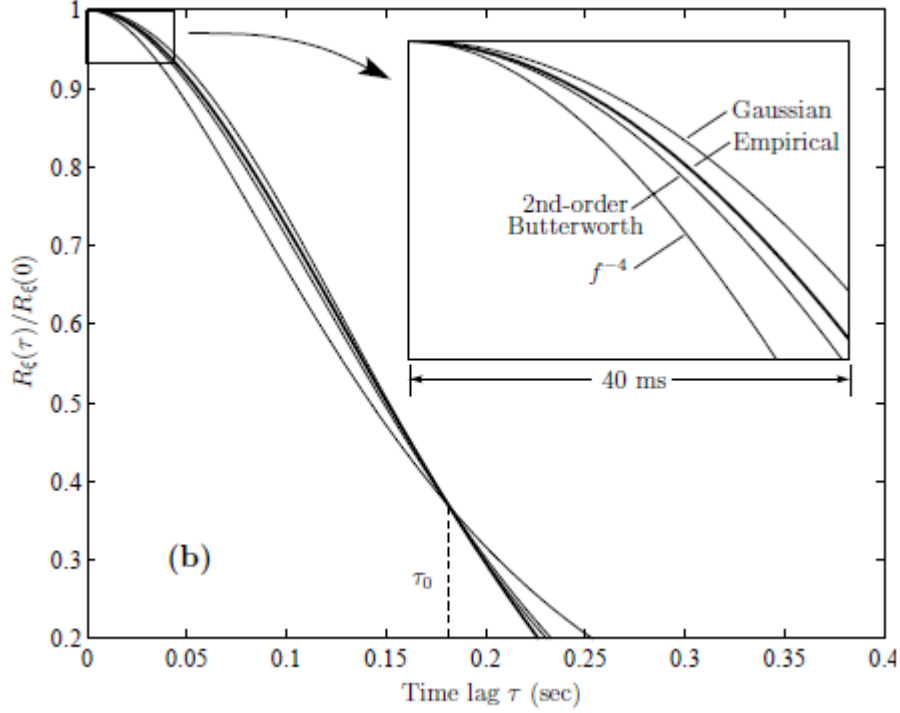


**Figure 5.3** (a) Empirical fading process spectrum  $S_{\xi}(f)$  with  $S_4 = 0.87$  in comparison with Gaussian and  $f^4$  and 2<sup>nd</sup> order butterworth filter. (b) Corresponding autocorrelation functions. Reprinted with permission from [43]

## 5.2 Scintillation simulator mechanization

The mechanization is the process of generating and combining two or more random data to get required output. The mechanization of Cornell scintillation model is given below in the figure 5.4. This model performs scintillation simulator mechanization that produces real scintillation time histories. From the block diagram, Gaussian white noise  $n(t)$  of zero-mean complex is routed through 2<sup>nd</sup> order butterworth filter whose amplitude response function is given by,

$$|H(f)| = 1 / \sqrt{1 + (f/B)^4} \quad (5.6)$$

Where  $B$  is filter bandwidth given by  $B = \beta / \sqrt{2\pi\alpha'}$  where  $\alpha'$  is required decorrelation time and  $\beta = 1.2396464$ . Let the filter noise be  $\tilde{\xi}(t)$  and corresponding variance be  $\sigma_{\xi}^2$ . Hence the direct component  $\tilde{z}$  is calculated by  $\tilde{z} = \sqrt{2(\sigma^2)\xi K}$  where  $K$  is estimated from equation (5.5) with  $S_4 \leq 1$  (from previous amplitude distribution section) and  $m = 1/S_4^2$ . After the summation of direct component  $\tilde{z}$  and  $\tilde{\xi}(t)$ , the result  $\bar{z}(t)$  is then normalized through  $\alpha = E[|\bar{z}(t)|]$  to generate synthetic scintillation time history  $z(t) = \bar{z} + \xi(t)$ .

The filter used in the model is discrete time filter and noise  $n(t)$  is generated through random noise generator as a sequence of independent samples. Scintillation

severity is found by choosing appropriate values of  $S_4$  and  $\tau_0$ . Strong scintillation is obtained by selecting high  $S_4$  and low  $\tau_0$  values as mentioned in Table 4.1. Very strong scintillation recorded in empirical wideband UHF shows the  $\tau_0$  value to be as low as 0.12 seconds. [44]

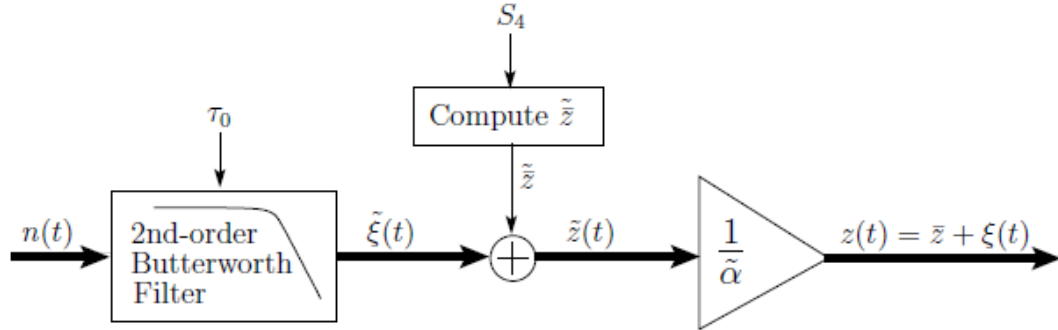


**Figure 5.4:** Schematic representation of Cornell Scintillation Model with thick black lines indicating complex signal transfer. Reprinted with permission from [43]

### 5.3 Model validation and conclusion

The method of validating Cornell scintillation model involves generating “truth” scintillation using phase screen model or by directly using data records from scintillation library. This validation method used in [25] wideband UHF data records from scintillation library whose stationary scintillation intervals higher than 150 seconds were selected. The reason for selecting wideband data is due to the presence of noise in GPS data and makes it convenient to test carrier tracking loops. Then the values of  $S_4$  and  $\tau_0$  are truth data are determined such that ten sets of synthetic scintillation data in equal length were produced based on  $S_4$  and  $\tau_0$  values of truth data. In the next step, truth data and ten synthetic scintillation data sets were routed into scintillation test bed with assumption of phase track loop noise bandwidth  $B_n = 10$  Hz and an accumulation interval  $T_a = 10$  ms for good tracking performance. Additive white noise is eliminated to study the effects of scintillation to make carrier to noise ratio infinite.

The responses of each scintillation data were stored as phase error variance  $\sigma_\phi^2$  and number of cycle slips  $N_s$  for each time interval and the mean and standard deviations of all the synthetic data were calculated. The results showed that phase tracking loop responses of both synthetic and truth scintillation data sets were identical [43]. Therefore, the results show that Cornell scintillation model is effective and realistic for carrier phase tracking loops. To conclude, Cornell scintillation model achieves the connection between differentially detected data bit errors and cyclic slips. The scintillation properties that work on maintaining phase lock are amplitude distribution and autocorrelation function. Studies from empirical library data sets and phase screen generated data sets suggest that amplitude distribution is represented as Rice distribution and autocorrelation function as 2<sup>nd</sup> order butterworth filter. These factors

make it convenient to build a scintillation simulator with  $S_4$  and  $\tau_0$  as inputs to get realistic synthetic scintillation output.

## **5.4 Various other scintillation models: benefits and drawbacks**

In this section, various other existing scintillation models to detect, analyse and mitigate scintillations were explained, though there is no information found in the papers to know if the models are available as open source. These models use different technique for determining and analyzing scintillation effects and explain benefits and drawbacks of the models.

### **5.4.1 Automatic ionospheric scintillation detector for GNSS**

In this model [52], the authors use Neyman Pearson Detector for detecting scintillations of different parameters that determines automatic threshold for evaluating probability of false alarm (Pfa) and probability of detection (Pd). This model was tested for strong scintillation activity occurred during 24<sup>th</sup> solar cycle during 2013 to 2014. The wavelet and Hilbert-Huang Transform (HHT) were used for decomposing and detecting the strength of the scintillation signal by implementing binary hypothesis testing [53]. The NP detector decides threshold value based on statistical description of signals with the help of probability density function (pdf). If the estimated value is greater than threshold value, then the signal contains scintillations and vice versa. The other task of wavelet and HHT is denoising and mitigating scintillated signal. The automatic scintillation detector has the advantage of performing during severe scintillation event. The HHT technique is more convenient for non-linear and non-stationary signals than the alternative wavelet transform. [52]

### **5.4.2 Modernized GNSS ionospheric scintillation and TEC Monitoring**

The Authors in the paper [54], introduces the Novatel's modern monitoring system that inspects ionospheric scintillation and total electron content (TEC) for determining amplitude and phase scintillation indices. This updated model "GPStation 6" has capacity to track multi-constellation, multi-frequency GNSS measurements. The advantage of this model is ensuring concrete, less noisy measurements and providing compatibility to GSV4004B receiver in all GNSS constellations for GPS L1/L2 signals. Another important benefit of GPStation-6 model is collecting amplitude and phase datas from SBAS (Satellite Based Augmentation System) satellites in equatorial regions.

### **5.4.3 Simulating ionospheric scintillation effects using low complexity technique**

The authors in [56], introduce a low complexity technique to simulate ionospheric scintillation effects. Similar to Cornell scintillation model, this model generates

amplitude correlated time series with Nakagami-m distribution and phase correlated Gaussian-distributed times series. Zhang algorithm used in Nakagami-m distribution creates correlated samples in the generation of complex time series. Zhang algorithm provides the principle of direct sum decomposition principle that finds statistical mapping between set of Gaussian signals and Nakagami process applied during implementation. In addition, the method uses Yule-Walker equation to generate Gaussian auto-regressive correlated signals.

## 6. GALILEO SYSTEM - OVERVIEW

In this chapter, brief description of Galileo satellite system and its signal modulation MBOC, Multiplexed binary offset carrier modulation are given. This chapter explains also the TUT MBOC simulator used for acquisition and tracking of Galileo E1 signals over multipath Nakagami-m fading channel. During transmission, the signal undergoes fading, addition of noise and also scintillation which is the focus of this thesis and the receiver results are studied by calculating LOS delay error.

### 6.1 Galileo signal characteristics

Galileo spectrum operates with four frequency bands and each band in turn, functions with different frequency based on the type of service. The frequency bands are categorized into lower L-band that consists of E5a frequency band with carrier frequency,  $f_c = 1176.45$  MHz and E5b frequency band with carrier frequency  $f_c = 1207.14$  MHz. The middle L-band consists of E6 frequency band with  $f_c = 1278.75$  MHz and upper L-band, E2-L1-E1 with  $f_c = 1575.42$  MHz [57]. The TUT MBOC simulators used in this thesis proposed in this paper generates Galileo E1-band signal.

### 6.2 Galileo Signal Modulation – MBOC

A consensus was reached by United states and European community to apply BOC(1,1) modulation for GPS L1C signals and Galileo E1 OS signals. To optimize the modulation with interoperability and compatibility, MBOC(6,1,1/11) was introduced to minimize interference from GPS L1C signals. This thesis uses CBOC, composite binary offset carrier modulation to implement MBOC modulation in the tracking algorithm. CBOC is used to reduce interference from GPS L1 signal.

#### 6.2.1 BOC Modulation

John W. Betz introduced the theory of BOC, Binary offset carrier modulation. BOC modulation multiplies the actual signal with rectangular sub-carrier of frequency  $f_{sc}$ , dividing the resulting spectrum into two parts. Therefore, the spectrum split offsets spectrum from central frequency and increases the power in higher frequencies enabling improved signal tracking performance [59]. BOC modulation is denoted as  $\text{BOC}(f_{sc}, f_c)$ , where  $f_{sc}$  is sub-carrier frequency and  $f_c$  is the chip frequency [58]. Sine-BOC time waveform is given by,

$$S_{\text{SinBOC}}(t) = \text{sign}(\sin(N_B \pi t / T_c)) \quad (6.1)$$

Cosine-BOC time waveform is given by,

$$S_{\text{CosBOC}}(t) = \text{sign}(\cos(N_B \pi t / T_c)) \quad (6.2)$$

where,  $N_B$  is BOC modulation order given by,  $N_B = 2(f_{sc} / f_c)$  and  $T_c$  is chip rate.

### 6.2.2 MBOC Modulation

MBOC(6,1,1/11) is the combination of BOC(1,1) and BOC(6,1) where main lobes of BOC(1,1) and BOC(6,1) are located at +/- 1MHz and +/- 6MHz respectively. The presence of BOC(6,1) makes additional higher frequency components in PSD. This characteristic makes benefit of using MBOC(6,1,1/11) over BOC(11) for the reason of additional power at higher frequencies. It is particularly useful in narrowband receivers to improve performance such as multipath tracking and acquisition [59]. MBOC has similar spectrum characteristic of BOC where BOC(6,1) consumes 1/11<sup>th</sup> of power and remaining power for BOC(1,1), Therefore PSD of MBOC(6,1,1/11) is given by,

$$G_{\text{MBOC}}(f) = \frac{1}{11}G_{\text{BOC}}(6,1)(f) + \frac{10}{11}G_{\text{BOC}}(1,1)(f) \quad (6.3)$$

### 6.2.3 CBOC Modulation

CBOC modulation is the implementation of MBOC modulation used by Galileo system. It is implemented by sum or difference of two weighted Sine Binary Offset Carrier Modulation [58].

$$S_{\text{CBOC}(+)}(t) = W_1 S_{\text{SinBOC}}(1,1)(t) + W_2 S_{\text{SinBOC}}(6,1)(t) \quad (6.4)$$

$$S_{\text{CBOC}(-)}(t) = W_1 S_{\text{SinBOC}}(1,1)(t) - W_2 S_{\text{SinBOC}}(6,1)(t) \quad (6.5)$$

where,  $W_1$  and  $W_2$  are two weights chosen as  $W_1 = \sqrt{10/11}$ , and  $W_2 = \sqrt{1/11}$ . CBOC(-) is used in Galileo E1 pilot signal and CBOC(+) is used in Galileo data signal.

## 6.3 TUT MBOC Simulator

The block diagram of TUT MBOC simulator is shown in Figure 6.1. The generated Galileo E1 (CBOC) signal is transmitted over a multipath Nakagami fading channel. The ideal ACF of MBOC-modulated codes (CBOC) were generated to compare it with the resulting correlation output, shown in Figure 6.2. Then scintillation with required scintillation intensity is added to the channel along with Additional White Gaussian Noise (AWGN). Here scintillation data histories generated from cornell scintillation toolbox are merged with tracking algorithm to simulate and achieve the

correlation output. Coherent integration is carried out to remove high frequency components using low pass filter, followed by Non-coherent integration to reduce noise floor. After signal processing, estimation of LOS delay based on the resulting correlation function is done by picking the first local maximum which is higher than the second peak of the ideal autocorrelation function.

### Time-Doppler acquisition mesh

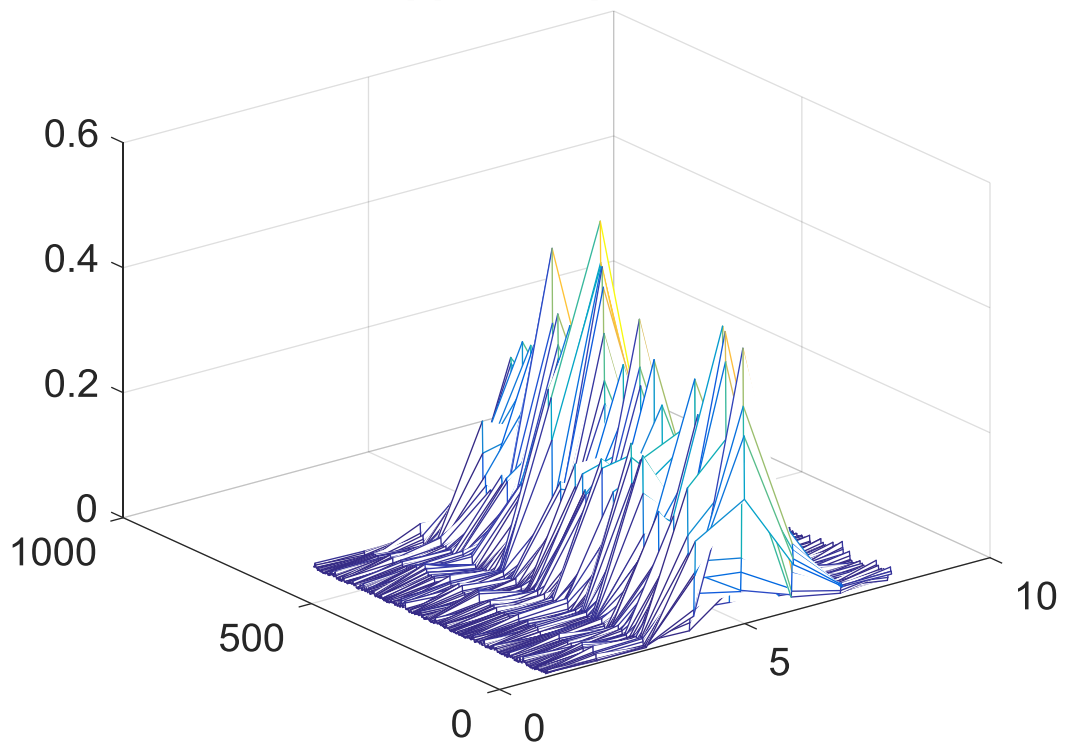


**Figure 6.2:** *An example plot of time-doppler mesh showing correlation output and main peak*

In the acquisition stage, once the LOS delay is determined, LOS error is calculated from the difference of true delay and estimated delay. Detection Probability ( $P_d$ ) is to measure the performance in acquisition and Root Mean Square Error (RMSE) is used in Tracking. An example of time-doppler mesh retrieved from the TUT MBOC Simulator is shown in Figure 6.2. It shows the correlation output and the position of the main peak that helps in estimating code delay error. Detection probability is estimated if the error found from the difference is lesser than delta error. Delta error is threshold error value that is set to indicate if the signal is detected when estimated LOS error is less than delta error. In this thesis, delta error is set as  $1/N_s/N_{BOC}$ , where  $N_s = 4$  is oversampling factor and  $N_{BOC}=12$  is overall BOC modulation order. Tracking is performed by calculating RMSE with the values of true delays and estimated delays.

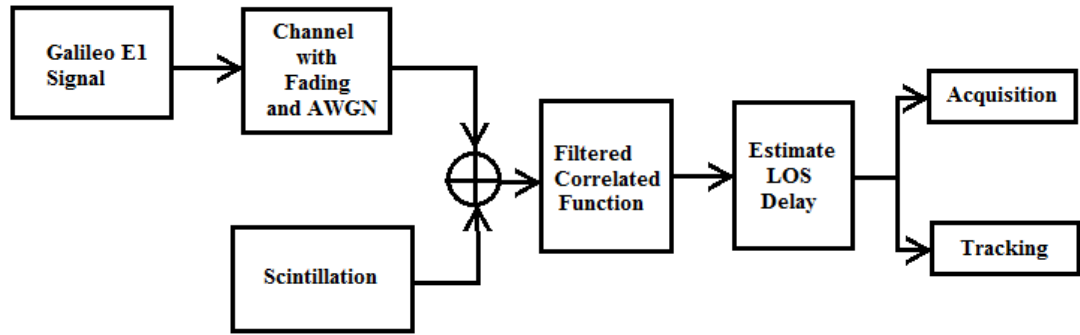


**Figure 6.1:** *The block diagram of TUT MBOC simulator*

## 7. RESULTS AND DISCUSSION

In this chapter, simulations from TUT MBOC simulator are presented and discussed. The Detection Probability ( $P_d$ ) and Root Mean Square Error (RMSE) of the estimated LOS delay are determined by executing the simulator over 1000 random points in order to get good statistics. Then the chapter focuses on comparative analysis of different error criterias namely, fading, AWGN and scintillation. The  $P_d$  is used as the performance criteria in acquisition and RMSE is used for tracking. In the end, performance of acquisition and tracking based on different scintillation levels are analyzed.

The scintillation time histories are generated using Cornell scintillation model and MBOC parameters and added to the channel along with other error criterias such as AWGN and fading. This is done in order to merge CSM with TUT MBOC simulator which is the focus of this thesis and to analyse the scintillated Galileo E1 signal. The simulation for both  $P_d$  and RMSE are plotted against increasing values of carrier to noise ratio ( $C/N_0$ ) in dB-Hz.

### 7.1 Performance analysis of scintillated E1 signal

In this section, simulation results for different number of channel paths 1, 4 and 10 are presented and comparative analysis among error criterias are performed. Scintillation parameter values are  $S_4 = 0.9$  and  $\tau_0 = 0.1$ , which denotes strong scintillation. The important parameters used for simulations are tabulated below,

Parameters	value
Overall BOC modulation order, $N_B$	12
Oversampling factor, $N_s$	4
Mobile speed in km/h	120
Spreading Factor <sup>1</sup>	101
Carrier-to-Noise ratio, ( $C/N_0$ ) in dB-Hz	20, 25, 30, 35, 40
Chip Rate in Hz	SF * 1000
Sampling Frequency in Hz	Chip Rate * $N_s$ * $N_B$

<sup>1</sup>A small SF was chosen for keeping the simulation time to a reasonable level. SF has little impact on the performance as we work with despread signal; strictly speaking, Galileo SF is 1023.

**Table 7.1:** *Important parameters and values used in TUT MBOC Simulator*

Figure 7.1 shows the detection probability of scintillated + fading signal whose  $P_d$  starts reducing when  $C/N_0$  is 25 dB-Hz. The  $P_d$  of scintillation only signal starts reducing at  $C/N_0 = 35$  dB-Hz. Hence, acquisition performance is less for scintillated signals than received signal with AWGN only. Figure 7.2 shows the tracking performance of scintillated signals against noise signal. RMSE of scintillated + fading signal shows the tracking error between 25 to 35 dB-Hz with maximum tracking error at  $C/N_0 = 30$  dB-Hz. From the figure 7.1, at  $P_d = 0.8$ , the difference of CNR of *AWGN only* and *scintillation only* curves is approximately equal to 0.5 dB-Hz, and the difference increases when the number of channel paths increase. Therefore, CNR of 0.5 dB-Hz is additionally required to get detection probability of  $P_d = 0.8$ , when the signal is affected by scintillation.

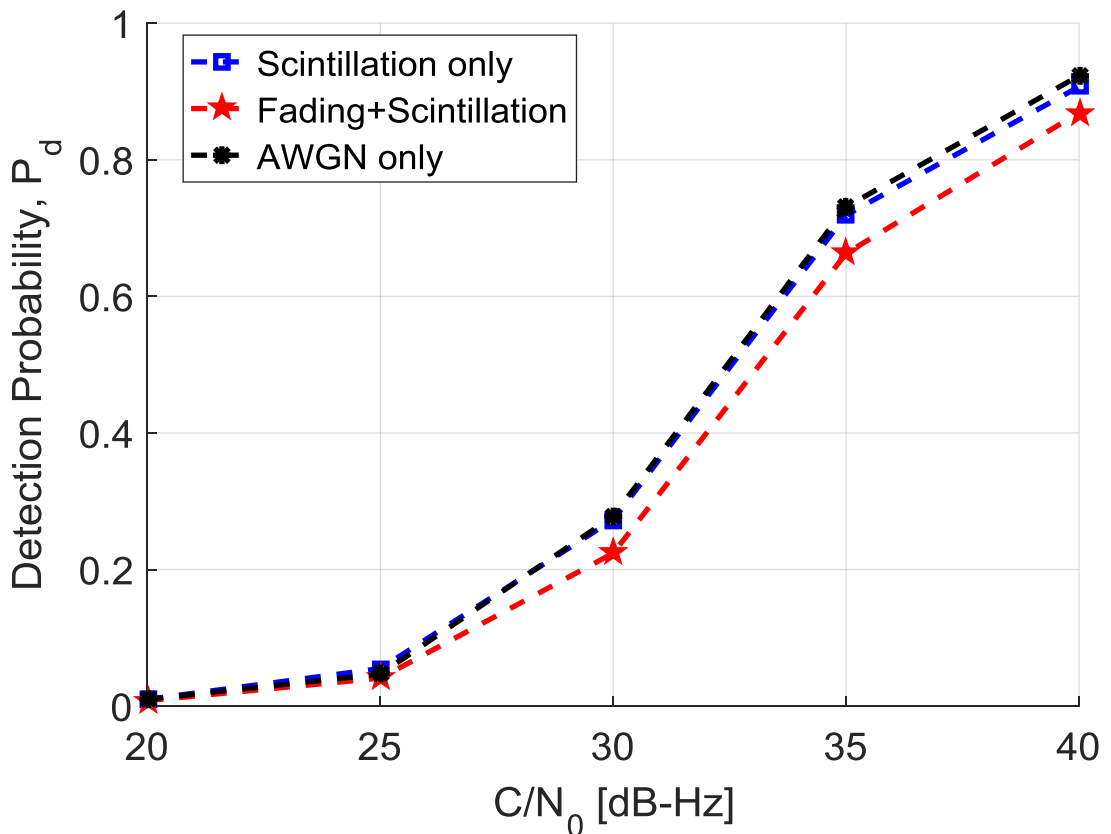


**Figure 7.1:** *Detection probability of the received signal, comparing Scintillation, Scintillation+fading and AWGN for one channel path.*

## 7.2 Impact of multipath fading channels

Figure 7.3 and Figure 7.4 shows the  $P_d$  and RMSE of signal for four channel paths. Comparing the results with Figure 7.1 and Figure 7.2, the performance of all the error criterias looks almost similar and the difference is that scintillation only and fading+scintillation, signals show poor performance during acquisition and tracking due to multiple channel paths. Therefore, increasing the number of channel paths have significant effect in the performance criteria of acquisition and tracking due to multipath errors. The impact is found more in simulations when number of channels increased to 10, as seen in Figure 7.5 and Figure 7.6. The  $P_d$  of the scintillated signals is lower than the values seen in the detection probability of Figures 7.1 and 7.3. Similarly, RMSE value of scintillated signals of 10 channels is higher than the RMSE values seen in the Figures 7.2 and 7.4.

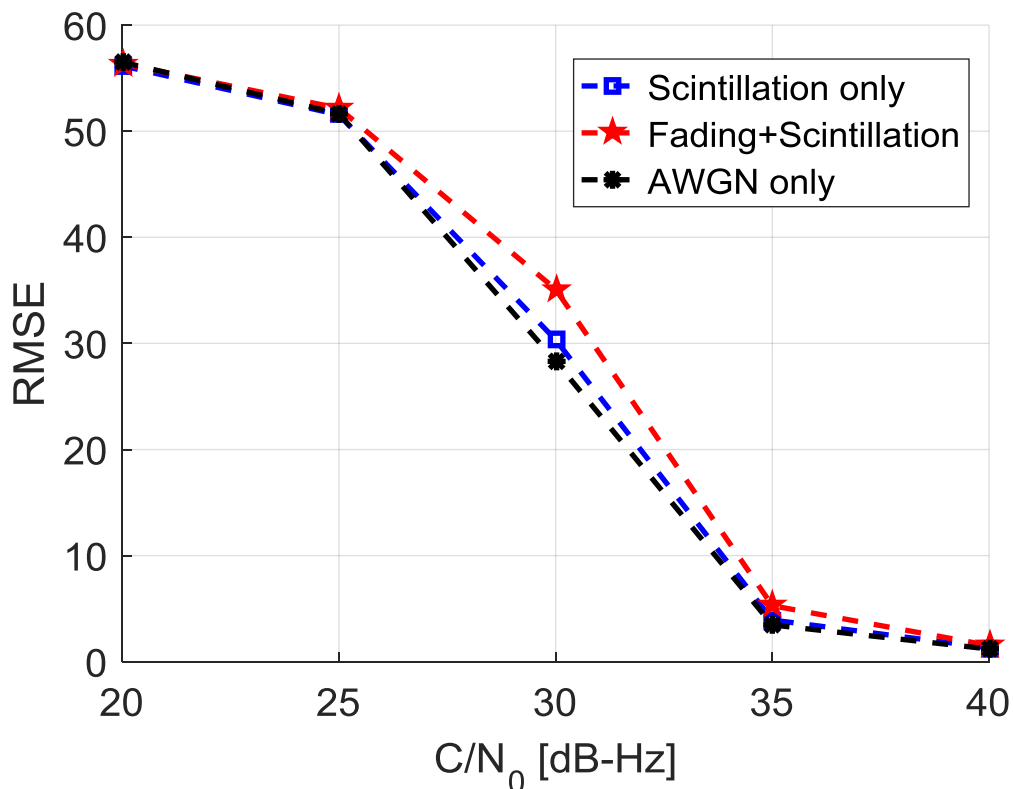


**Figure 7.2:** RMSE of the received signal in meters (m), comparing Scintillation, Scintillation+fading and AWGN for one channel path.

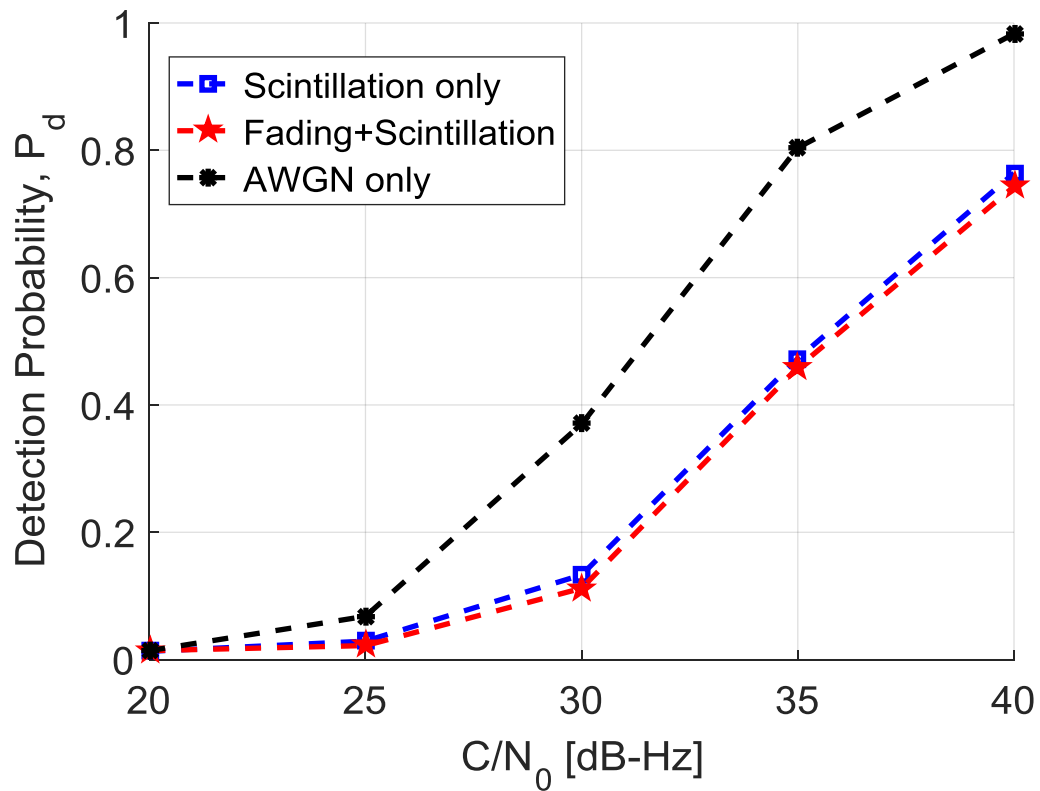


**Figure 7.3:** Detection probability of the received signal, comparing Scintillation, Scintillation+fading and AWGN for four channel paths.

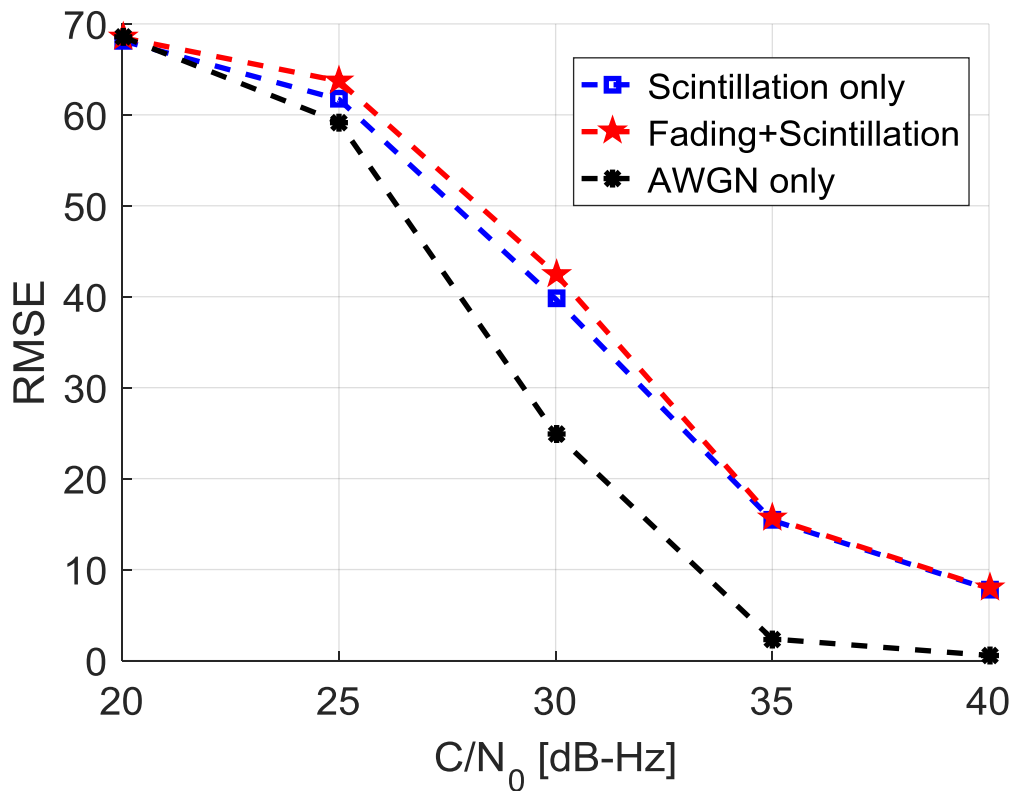


**Figure 7.4:** RMSE of the received signal in meters (m), comparing Scintillation, Scintillation+fading and AWGN for four channel paths.

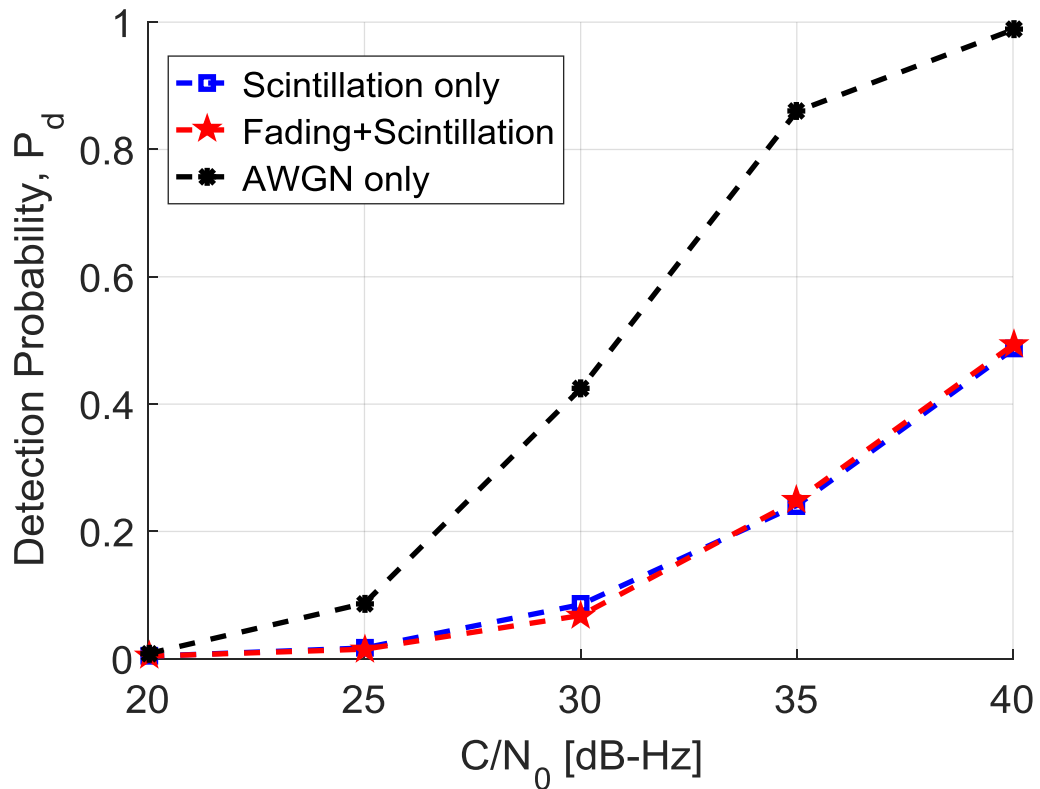


**Figure 7.5:** Detection probability of the received signal, comparing Scintillation, Scintillation+fading and AWGN for 10 channel paths.

From the figure 7.3, at  $P_d = 0.7$ , the difference in CNR of AWGN signal and scintillation only for 4 channel paths is 6 dB-Hz. Therefore, CNR of 6 dB-Hz is degraded when the signal is affected by scintillation. From the figure 7.5, if the number of channel paths is increased to 10, CNR is degraded more to 9 dB-Hz at  $P_d = 0.5$ , due to multipath errors. To mitigate multipaths errors at the receiver, various correlators are used to estimate the accurate shape of multipath faded correlated function. Multipath Estimating Delay Lock Loop (MEDLL) can be used to estimate the parameters namely, amplitudes, phase and delays in order to reduce multipath errors at receiver output [54].

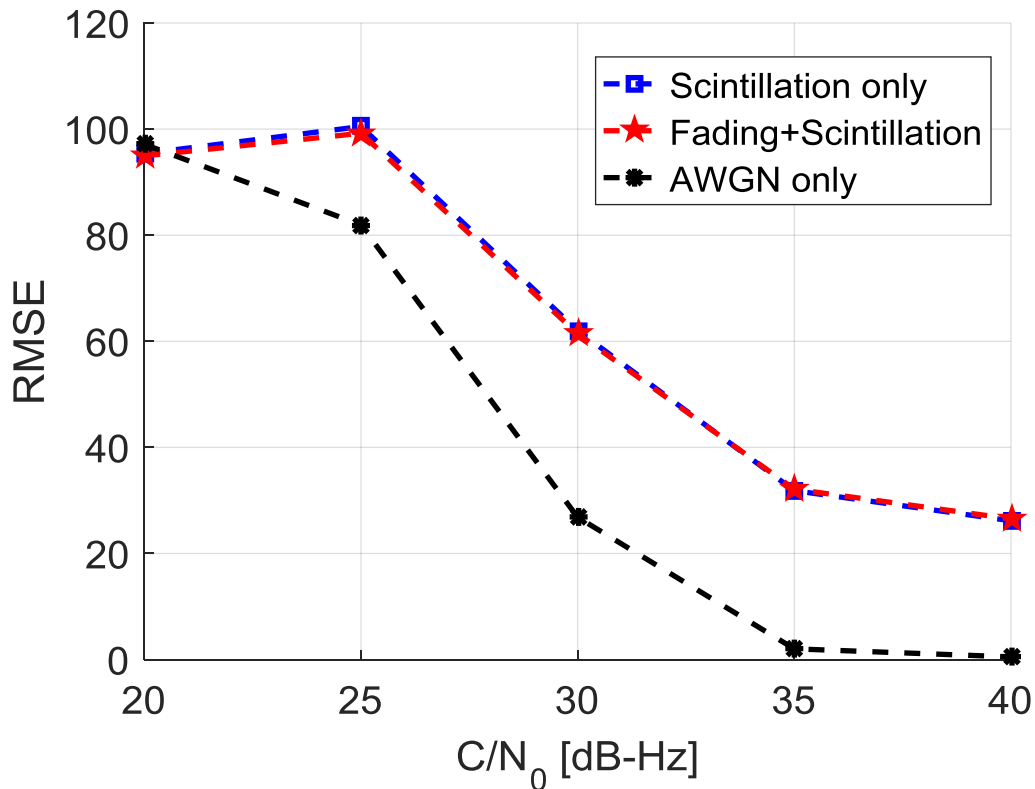


**Figure 7.6:** RMSE of the received signal in meters (m), comparing Scintillation, Scintillation+fading and AWGN for 10 channel paths.

### 7.3 Performance analysis of different scintillation levels

This section focuses on simulations of various scintillation levels in order to analyse the performance of acquisition and tracking. The table 7.2 shows the values of scintillation intensity and decorrelation time used in the simulations for different scintillation levels.

Scintillation level	S <sub>4</sub> value	$\tau_0$ (sec)
weak	0.9	0.2
moderate	0.4	0.8
strong	0.15	1.5

**Table 7.2:**  $S_4$  and  $\tau_0$  values for various scintillation levels used in the simulations.

#### 7.3.1 Analysis of scintillation levels with fading

The  $P_d$  and RMSE for different scintillation levels with one channel path fading are shown in Figure 7.7 and Figure 7.8 respectively. The simulation results show that the strong scintillation curve undergoes performance degradation, as the value of  $P_d$  is lesser than weak and moderate scintillations. The RMSE value of strong scintillation is higher than other scintillation levels that show lower value than strong scintillation. To further

understand and compare the performance evaluation,  $P_d$  and RMSE of AWGN only indicates good acquisition and tracking performance than scintillation plots.

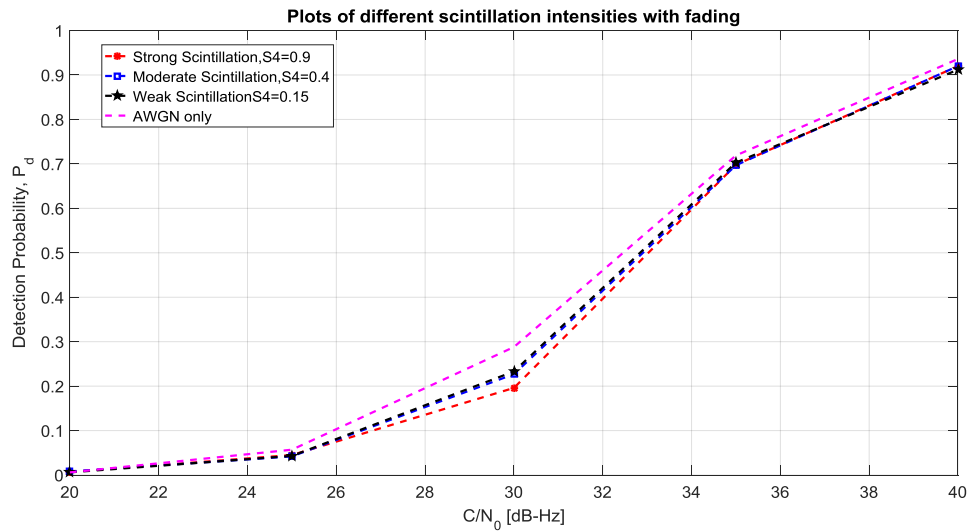


**Figure 7.7:** The comparison of  $P_d$  of weak, moderate and strong scintillations with fading for one channel path.

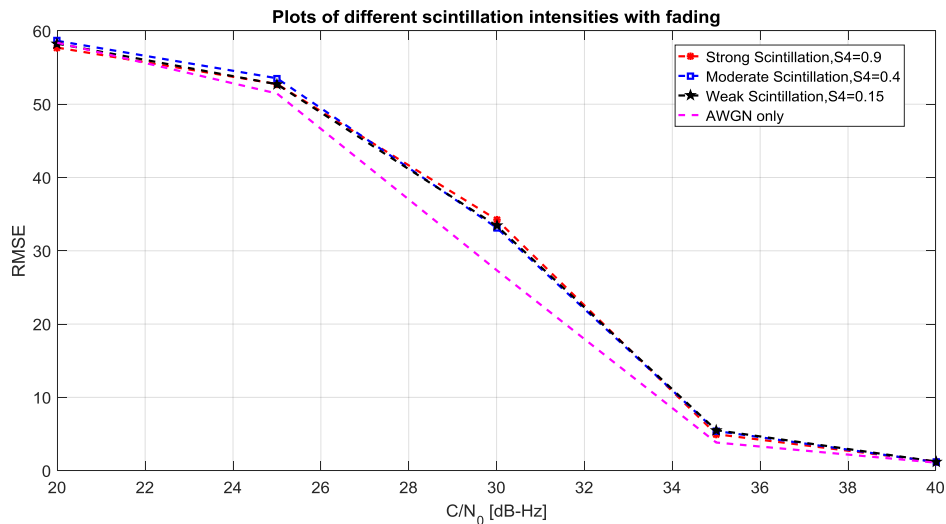


**Figure 7.8:** The comparison of  $RMSE(m)$  of weak, moderate and strong scintillations with fading for one channel path.

The acquisition and tracking of various scintillation levels, namely weak, moderate and strong scintillations are shown in Figures 7.9 and 7.10. The number of channel paths used in these figures are four. Similar to previous figures 7.3 and 7.4, the increase in number of channel paths decreases the performance of acquisition and tracking. The values of  $P_d$  in Figure 7.9 is lower than Figure 7.7 for all the CNR values and the value of RMSE in Figure 7.10 is higher than Figure 7.8 for all the CNR values. The difference in CNR for strong and weak scintillation is found from the plots to know how much the signal is degraded due to increased scintillation severity. At  $P_d = 0.7$ , from the figure 7.7, the difference in CNR is found negligible when number of channel path is equal to

one, but the difference in CNR is approximately equal to 1 dB-Hz when number of channel paths is increased to 4, which can be seen in figure 7.9.

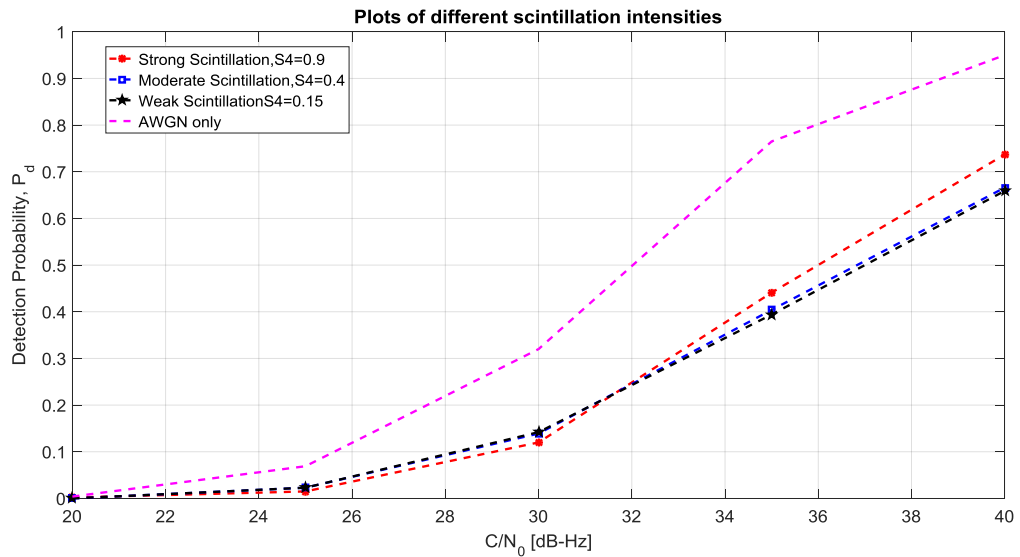


**Figure 7.9:** The comparison of  $P_d$  of weak, moderate and strong scintillations with fading for four channel paths.

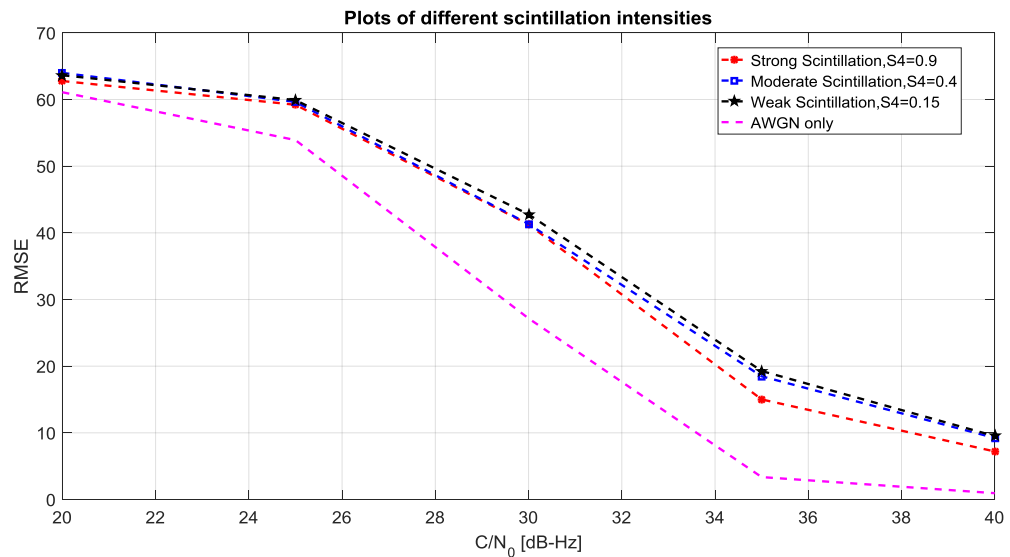


**Figure 7.10:** The comparison of  $RMSE(m)$  of weak, moderate and strong scintillations with fading for four channel paths.

### 7.3.2 Analysis of scintillation levels without fading

Figures 7.11 and 7.12 show the simulation results that displays detection probability and RMSE of different scintillation levels without fading. The value of  $P_d$  is almost same for all CNR values except at 35 dB-Hz where it shows slightly lesser  $P_d$  value. The scintillation levels shows similar performance when fading is excluded during

simulation. The RMSE value also shows similar result where the RMSE value is slightly higher for strong scintillation comparing to other scintillation levels.

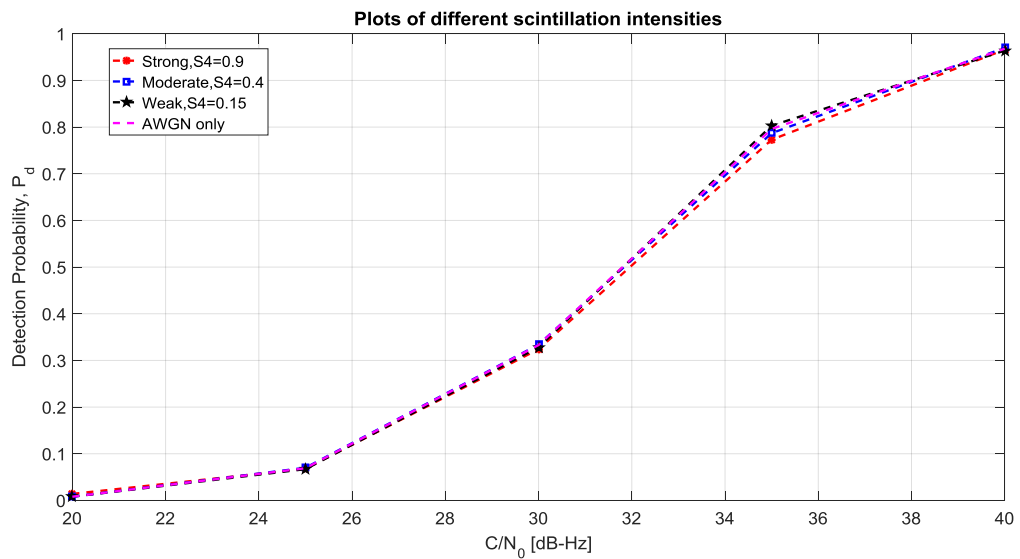


**Figure 7.11:** The comparison of  $P_d$  of weak, moderate and strong scintillations without fading for one channel path.

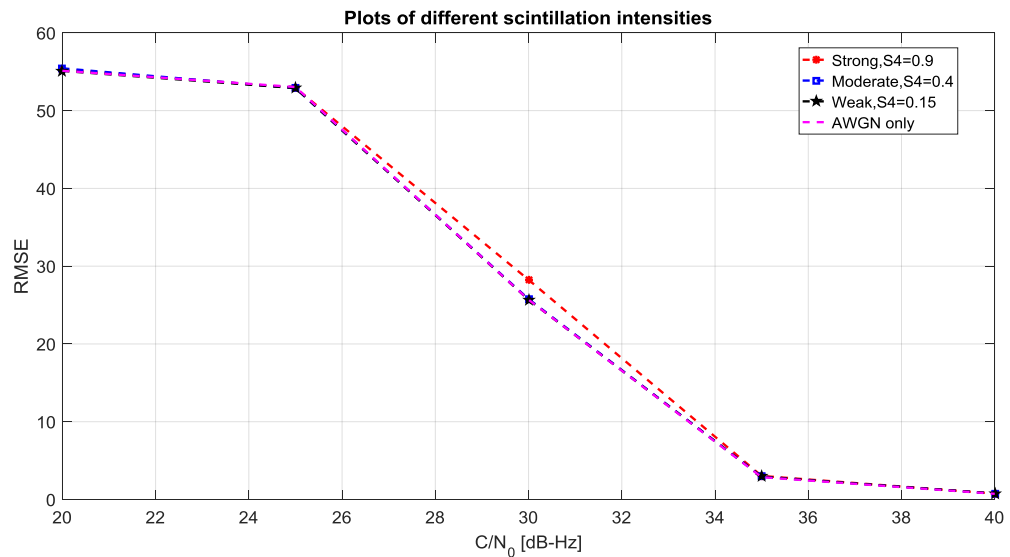


**Figure 7.12:** The comparison of  $RMSE(m)$  of weak, moderate and strong scintillations without fading for one channel path.

The figures 7.13 and 7.14 shows the  $P_d$  and  $RMSE$  with four channel paths whose acquisition and tracking performance is lower comparing to one channel path. As we did earlier, to determine the amount of signal degradation when scintillation severity is increased, the difference in CNR of strong and weak scintillation is estimated. From the figure 7.11, at  $P_d = 0.7$ , the difference in CNR is about 0.3 dB-Hz, whereas increase in number of channel paths to 4, degrades the CNR by 2 dB-Hz which is seen in figure 7.13.

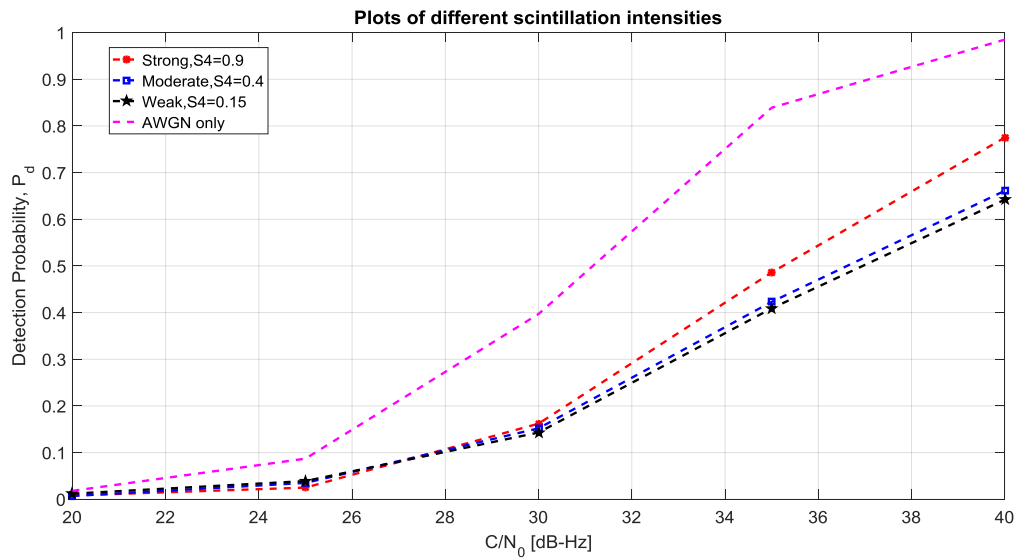


**Figure 7.13:** The comparison of  $P_d$  of weak, moderate and strong scintillations without fading for four channel paths.

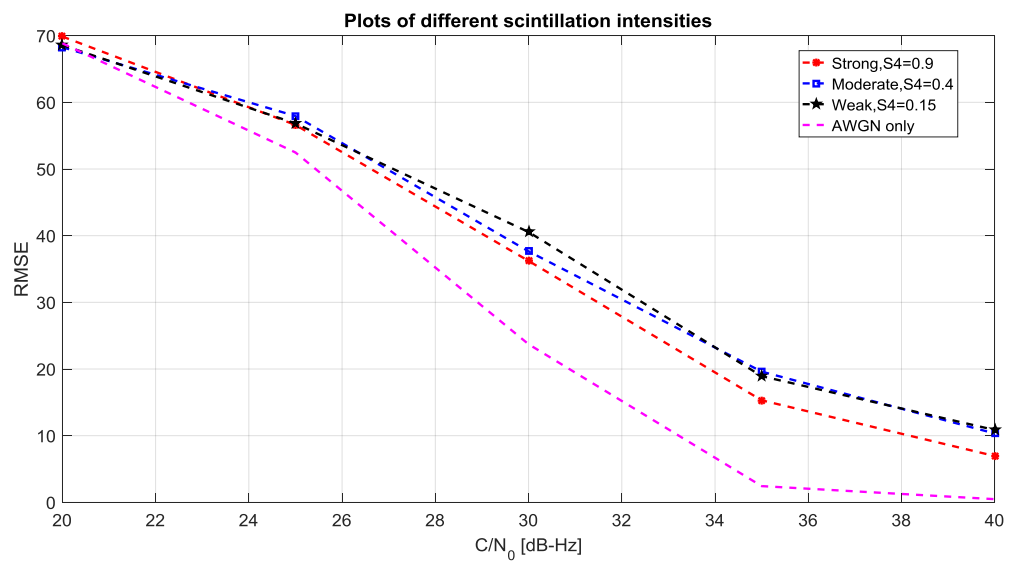


**Figure 7.14:** The comparison of  $RMSE(m)$  of weak, moderate and strong scintillations without fading for four channel paths.

## 8. CONCLUSION

This chapter summarizes the focus of this thesis and concludes the work with the findings of simulation results. In this thesis, two toolboxes namely Cornell scintillation toolbox and TUT MBOC simulator were studied and appropriate changes to the MBOC parameters were done to merge the toolboxes. The research was done to learn about characteristics of scintillation and its parameters Scintillation Intensity ( $S_4$ ) and decorrelation time ( $\tau_0$ ). In addition, scintillation effects on acquisition and tracking were studied to analyze the performance criterias, Detection Probability ( $P_d$ ) and Root Mean Square Error (RMSE) respectively.

The TUT MBOC simulator implements CBOC modulation to reduce interference from GPS L1 signal, as the simulator generates Galileo E1 signal, which is transmitted over Nakagami-m fading channel along with scintillation to estimate LOS delay from corrupted correlation function. The main peak of the resulting correlation function indicates the presence of the signal. Then, the simulator acquires and tracks the signal with error which undergoes further processing to create connection between satellite and user.

The obtained simulation results showed the performance degradation of acquisition and tracking when strong scintillation perturbed the Galileo signal. The number of channel paths also degraded the performance of the receiver due to multipath error. We noticed that scintillation deteriorates the acquisition performance compared to AWGN case with 0.5 dB in single path, 6 dB in four paths, and 9 dB in 10 path channels. We also noticed that a strong scintillation can deteriorate the acquisition performance with upto 2 dB compared to a weak scintillation in 4 path channels.

Several correlators can be used in the receiver to mitigate the multipath errors of corrupted correlation function. The simulation results were also obtained for different scintillation levels namely, weak, moderate and strong scintillations. The detection probability and RMSE results were almost similar for all levels of scintillation with slight variation for strong scintillation. The future works may include the research for learning the cause of slight variation for strong scintillation comparing to weak and moderate scintillations. In addition, research can be done for mitigating multipath errors when using more number of channel paths.

---

## REFERENCES

- [1] Kintner Jr, P.M., Humphreys, T.E., Hinks, J.C., "GNSS and Ionospheric Scintillations," 2009. [Online]. Available: <http://www.insidegnss.com/auto/julyaug09-kintner.pdf>. [Accessed 15 Jan 2017].
- [2] Strangeways, H. J., Gherm, V. E., Zernov, N. N., Modeling and mitigation of the effect of scintillations on GPS, Zadar, 2007, pp. 69-73.
- [3] Gleason S., Gebre-Egziabher D., GNSS Applications and Methods, London: Artech House, 2009.
- [4] "European Global Navigation Satellite Systems Agency," The European GNSS Supervisory Authority (GSA), 12 July 2004. [Online]. Available: <https://www.gsa.europa.eu/european-gnss/what-gnss>. [Accessed 22 Feb 2017].
- [5] Wellenhof, B.H., Lichtenegger, H., Wasle, E., GNSS – Global Navigation Satellite Systems, Austria: Springer-Verlag Wien, 2008, p. 501.
- [6] Lohnert E., Wittmann E., Pielmeier J. and Sayda F., Paramount public safety & commercial Info-Mobility applications & Services in the Mountains, Salt Lake City, UT: ION GPS 2001, 2001, pp. 319-325.
- [7] Feng, Y., "Combined Galileo and GPS: A Technical Perspective," *Journal of Global Positioning Systems*, vol. II, no. 1, pp. 67-72, 2003.
- [8] Lohan, E.S., *Signal Processing for Mobile Positioning*, Tampere University of Technology, p. 90.
- [9] Ward, P.W., Betz, J.W., Hegarty, C.J., "Understanding GPS Principles and Applications," in *Satellite Signal Acquisition, Tracking, and Data Demodulation*, 2nd ed., pp. 153-241.
- [10] Pini, M., Falco, G., Presti, L.L., " Estimation of Satellite-User Ranges Through GNSS Code Phase Measurements," in *Global Navigation Satellite Systems: Signal, Theory and Applications*, In Tech, 2012, pp. 107-126.
- [11] Psiaki, M., Humphreys, T.E., Cerruti, A., Ledvina, B., Mannucci, A., Gary, D., de Paula, E., "A Beginner's Guide to Space Weather and GPS," Cornell University, 2008.
- [12] Kintner, P. M., Ledvina, B. M., de Paula, E. R., "GPS and ionospheric scintillations," *Space Weather*, no. 10.1029/2006SW000260, 2007.
- [13] Kintner, P.M., Ledvina, B.M., "The ionosphere, radio navigation, and global navigation," *Adv. Space Res.*, vol. 35, no. 5, pp. 788-811, 2005.

- 
- [14] Boscher, D., Carvalho, F., Fabbro, V., Lemorton, J., Fleury, R., "Modelling ionospheric effects for L band GNSS receivers at high latitudes," in *Antennas and Propagation (EuCAP) 8th European Conference*, France, 2014.
- [15] "European Space Agency," European Space Agency(esa), [Online]. Available: [http://www.esa.int/Our\\_Activities/Space\\_Science/What\\_are\\_solar\\_flares](http://www.esa.int/Our_Activities/Space_Science/What_are_solar_flares). [Accessed 17 05 2017].
- [16] Cerruti, A.P., Kintner, P.M., Gary, S.E., Lanzerotti, K.J., de Paula, E., Vo, H., "Observed solar radio burst effects on GPS/Wide Area Augmentation System carrier-to-noise ratio," *Space Weather*, vol. 4, no. doi:10.1029/2006SW000254, 2006, 2006.
- [17] Kintner, P.M., Ledvina, B.M., de Paula, E.R., Kantor, I.J., "The size, shape, orientation, speed, and duration of GPS equatorial anomaly scintillations," *Radio Sci.*, no. 10.1029/2003RS002878, p. 39, 2004.
- [18] Rino, C.L., "A power law phase screen model for ionospheric scintillation (1. Weak Scatter)," *Radio Science*, vol. 14, no. 6, pp. 1135-1145, 1979.
- [19] Humphreys, T.E., Psiaki, M.L., Kintner, P.M., "Modeling the Effects of Ionospheric Scintillation on GPS Carrier Phase Tracking," *IEEE Transactions on Aerospace and Electronic Systems*, vol. 46, no. DOI: 10.1109/TAES.2010.5595583, pp. 1624-1637, 2010.
- [20] Morrissey, T. N., Shallberg, K. W., Van Dierendonck, A. J., Nicholson, M. J., "GPS receiver performance characterization under realistic ionospheric phase scintillation," *Radio Sci.*, vol. 39, pp. 1-18, 2004.
- [21] Fremouw, E.J., Livingston, R.C., Miller, D.A., "On the statistics of scintillating signals," *Journal of Atmospheric and Terrestrial Physics*, vol. 42, no. 10.1016/0021-9169(80)90055-0, pp. 717-731, 1980.
- [22] Fremouw, E.J., Leadabrand, R.L., Livingston, R.C., Cousins, M.D., Rino, C.L., "Early results from the DNA Wideband Satellite experiment - Complex-scintillation signal," *Radio Science*, vol. 13, no. 10.1029/RS013i001p00167, pp. 167-187, 1978.
- [23] Humphreys, T. E., Ledvina, B. M., Psiaki, M. L., Kintner, P. M., "Analysis of ionospheric scintillations using wideband GPS L1 C/A signal data," *Proc. ION GNSS 2004, Long Beach, California: Institute of Navigation*, pp. 399-407, 2004.
- [24] J. Aarons, "Global morphology of ionospheric scintillations," in *Proceedings of the IEEE*, 1982.
- [25] Humphreys, T.E., Edwin, T., *Modeling Ionospheric Scintillation and its Effects on GPS Carrier Tracking Loops and two other Applications of Modeling and Estimation*, A Dissertation: Presented to the Faculty of the Graduate School of Cornell University, 2008.
- [26] Yeh, K.C., Liu, C.H., "Radio wave scintillations in the ionosphere," *Proceedings of the IEEE*, vol. 70, no. 4, pp. 324-360, 1982.

- 
- [27] Alouini, M., Simon, M.K., "Digital Communications over Fading Channels," in *Chapter 2*, New York: Wiley, 2000.
- [28] M. Nakagami, "The m-distribution: A general formula of intensity distribution of rapid fading," in *Statistical Methods in Radio Wave Propagation*, New York: Pergamon, W. C. Hoffman Ed., 1960, pp. 3-36.
- [29] Akos, D. M., Normark, P., Lee, J.T., Gromov, K. G., Tsui, J. B., Schamus, J., "Low power global navigation satellite system (GNSS) signal detection and processing," in *Proceedings of the 13th International Technical Meeting of the Satellite Division of The Institute of Navigation*, Salt Palace Convention Center, Salt Lake City, 2000.
- [30] Silva, D.M., "Comparison of Acquisition Methods for Software GPS Receiver," in *Proceedings of the 13th International Technical Meeting of the Satellite Division of The Institute of Navigation*, Salt Palace Convention Center, Salt Lake City, 2000.
- [31] Lin, D.M., Tsui, J.B., Howell, D., "Direct P(Y)-Code Acquisition Algorithm for Software GPS Receivers," in *Proceedings of the 12th International Technical Meeting of the Satellite Division of The Institute of Navigation*, Savannah GA, 1999.
- [32] Knight, M., Finn, A., "The effects of ionospheric scintillations on GPS," in *Proceedings of the 11th International Technical Meeting of the Satellite Division of The Institute of Navigation*, Nashville, TN, 1998.
- [33] Tsui, J. B. Y., *Acquisition of GPS C/A Code Signals in Fundamentals of Global Positioning System Receivers: A Software Approach*, John Wiley & Sons, Inc., 2005.
- [34] Ahmed, A., "Scintillation on Global Navigation Satellite Signals and its Mitigation," School of Electrical and Electronic Engineering, Newcastle University, Newcastle, 2015.
- [35] Psiaki, M. L., "Block Acquisition of Weak GPS Signals in a Software Receiver," in *Proceedings of the 14th International Technical Meeting of the Satellite Division of The Institute of Navigation*, Salt lake City, 2001.
- [36] Elmas, G.Z., Aquino. M., Forte, B., "The Impact of Ionospheric Scintillation on the GNSS Receiver Signal Tracking Performance and Measurement Accuracy," Institute of Engineering Surveying and Space Geodesy, Nottingham, 2011.
- [37] Conker, R.S., El-Arini, M.B., Hegarty, C.J., Hsiao, T., "Modeling the effects of ionospheric scintillation on GPS/SBAS availability," *Radio Science*, 2003.
- [38] Humphreys, T.E., Psiaki, M.L., Hinks, J.C., Hanlon, B.O., Kintner, P.M., "Simulating Ionosphere-Induced Scintillation for Testing GPS Receiver Phase Tracking Loops," *IEEE JOURNAL OF SELECTED TOPICS IN SIGNAL PROCESSING*, vol. 3, no. 4, pp. 707-715, 2009.
- [39] Humphreys, T. E., Psiaki, M. L., Ledvina, B. M., Cerruti, A. P., Kintner, P. M.,

- "Characterization of severe ionospheric scintillation and its effect on GPS carrier phase tracking," in *IEEE Transactions on Aerospace and Electronic Systems*, 2007.
- [40] Hegarty, C., El-Arini, M. B., Kim, T., Ericson, S., "Scintillation modeling for GPS-wide area augmentation system receivers," *Radio Science*, vol. 36, no. 5, pp. 1221-1231, 2001.
- [41] Be'niguel, Y., Hamel, P., "A global ionosphere scintillation propagation model for equatorial regions," no. 10.1051/swsc/2011004, 2011.
- [42] Rino, C.L., Owen, J., "Numerical simulations of intensity scintillation using the power law phase screen model," *Radio Science*, vol. 19, pp. 891-908, 1984.
- [43] Umeki, R., Liu, C.H., Yeh, K.C., "Multifrequency spectra of ionospheric amplitude scintillations," *Journal of Geophysical Research*, vol. 82, pp. 2752-2760, 1977.
- [44] Myers, W. J., Gjeldum, R.J., Liu, C.H., Yeh, K. C., "A study of ionospheric scintillations of phase and quadrature components," *Journal of Geophysical Research*, vol. 84, pp. 2039-2048, 1979.
- [45] Pidwerbetsky, A., "Simulation and analysis of wave propagation through random media," Ph.D. dissertation, Cornell University, 1988.
- [46] Dana, R.A., "Effects of ionospheric scintillation on differential demodulation of GPS data," *IEEE Transactions on Aerospace and Electronic Systems*, vol. 33, no. 3, pp. 893-902, 1997.
- [47] Devanaboyina, V.R., Gampala, S., Lee, J., "Automatic ionospheric scintillation detector for global navigation satellite system receivers," Global Navigation Satellite Systems Laboratory, Department of Aerospace Engineering, Daejeon, Republic of Korea, 2014.
- [48] Kolawole, M.O., "Radar systems, peak detection and tracking," Elsevier, 2002.
- [49] Shanmugam, S., Jones, J., Van Dierendonck, A.J., MacAulay A., "Evolution to Modernized GNSS Ionospheric Scintillation and TEC Monitoring," NovAtel Inc., Calgary, Alberta, Canada.
- [50] Nunes, F.D., Sousa, F. M. G., "Practical Simulation of GNSS Signals in the Presence of Ionospheric Scintillation," 978-1-4799-3320-4/14/IEEE, Lisboa, 2014.
- [51] Hein, G.W., Godet, J., Issler, J.L., Martin, J.C., Erhard, P., Rodriguez, R.L., Pratt, T., "Status of Galileo Frequency and Signal Design," in *Proceedings of the 15th International Technical Meeting of the Satellite Division of The Institute of Navigation (ION GPS 2002)*, Portland, 2002.
- [52] Shen, Y., Cao, X., "Research and Simulation on MBOC Modulated Navigational Signal," National Mobile Communications Research Laboratory, Nanjing, China.
- [53] Lohan E.S., "Spread Spectrum Techniques, Lecture 11," in *Satellite Based Positioning II*, Tampere, Tampere University of Technology.
- [54] Nee, R.D.J.V., "The Multipath Estimating Delay Lock Loop," In *IEEE Second International Symposium on Spread Spectrum Techniques and Applications*,

---

Yokohama, 1992.

- [55] Humphreys, T. E., Psiaki, M. L., Ledvina, B. M., Kintner Jr, P. M., "GPS Carrier tracking loop performance in the presence of ionospheric scintillations," in *Proceedings of ION GNSS 2005*, Long Beach, CA: Institute of Navigation, 2005.